Composites: Part A 200 (2026) 109306

Contents lists available at ScienceDirect

Composites Part A

journal homepage: www.elsevier.com/locate/compositesa

Rate-dependent 3D forming simulation of thermoplastic composite materials using visco-hyperelastic material modeling and 3D hexahedral solid-shell elements

Johannes Mitsch *, Bastian Schäfer, Luise Kärger *

Lightweight Engineering, Institute of Vehicle System Technology (FAST), Karlsruhe Institute of Technology (KIT), Karlsruhe, 76131, Germany

ARTICLE INFO

Keywords:
Finite Element Analysis
Process simulation
Thermoforming
Composite Forming Simulation
Solid-shell

ABSTRACT

The Finite Element Method is a widely applied approach for predicting manufacturing effects in the thermoforming process of fiber-reinforced composite materials. The majority of macroscopic simulation approaches are based on shell elements with two-dimensional (2D) stress states and provide efficient predictions of the forming process of composite materials. However, they lack the ability to capture through-thickness behavior due to their dimensional limitations. The present study proposes a three-dimensional (3D) solid-shell element formulation that incorporates rate-dependent material modeling thus enabling the simulation of the thermoforming process of thermoplastic composites. The solid-shell element formulation provides a locking-free formulation, an hourglass stabilization technique to prevent zero-energy modes, a reduced integration scheme, and the consideration of a rate-dependent material behavior. An analysis of the correspondence between the material parameters of the 3D solid-shell element and an experimentally validated 2D approach indicates that the 2D approach can effectively be employed to characterize in-plane and bending material parameters for the 3D solid-shell element formulation, streamlining and accelerating its material parameter identification process. The parameterization of the nonlinear compaction behavior of the solid-shell element exhibits a strong correlation with experimental results from existing literature. Finally, the solid-shell element is utilized to simulate the thermoforming process of a thermoplastic tape, yielding results that closely match those obtained from a 2D approach. The predicted thickness distribution, determined by the new 3D solid-shell, agrees well with the expected results, confirming the validity and practical potential of the proposed approach.

1. Introduction

1.1. Motivation

The quality of continuous fiber-reinforced thermoplastic (CoFRTP) components is significantly influenced by the manufacturing process and the process configuration. The significance of process parameters such as temperature [1,2], grippers [3–5], and initial fiber orientation [6,7] on the final part geometry is well documented. However, the experimental optimization of these parameters can be time-consuming and costly. Therefore, the Finite Element Method (FEM) has become an essential tool for designing and optimizing the forming processes of CoFRTP, as it enables a virtual optimization of the manufacturing process [8,9].

Over the past two decades, significant progress has been made in the development of simulation tools for the thermoforming of continuous fiber-reinforced plastics [10–13]. Despite these advancements, the majority of macroscopic simulation approaches rely on shell elements with 2D stress states [9]. Given the characteristic thin-walled geometry of CoFRTP sheets, these models have been proven efficient in capturing in-plane membrane behavior, out-of-plane bending, and inter-ply interactions. Consequently, they possess the capability to accurately predict the geometry of the final part, fiber orientation and wrinkling phenomena [11]. However, these elements inherently cannot model the through-thickness behavior of CoFRTPs, e.g., out-of-plane compaction or through-thickness thermal gradients. This constraint is attributed to the absence of the required degrees of freedom to represent through-thickness deformation and through-thickness temperature distributions. This limitation becomes critical when predicting final part thickness, local fiber volume content, press forces or locally varying material properties due to heating or contact conditions. These parameters are essential for optimizing the forming process and are crucial for subsequent simulation steps, e.g. the warpage simulation [14]. To

* Corresponding authors.
E-mail addresses: johannes.mitsch@kit.edu (J. Mitsch), luise.kaerger@kit.edu (L. Kärger).

https://doi.org/10.1016/j.compositesa.2025.109306
Received 16 July 2025; Received in revised form 10 September 2025; Accepted 14 September 2025
Available online 20 September 2025

enable material modeling in thickness direction, 3D finite elements are required [15]. However, standard 3D finite elements are vulnerable to numerical locking phenomena and therefore are not suitable for the simulation of the forming process of CoFRTP. Consequently, the development of a specialized 3D finite element formulation is necessary to enable the simulation of the forming process of CoFRTPs.

1.2. Related work

1.2.1. Forming simulation of CoFRTPs using two-dimensional element approaches

CoFRTPs exhibit high tensile stiffness along the fiber direction, due to the presence of quasi-inextensible fibers. In contrast, the matrix material adds strong time- and temperature-dependent behavior. Despite their high tensile stiffness, CoFRTPs show relatively low resistance to bending deformation. This is attributed to the low transverse shear stiffness in pre-impregnated textiles resulting in dominant relative motion between fibers during bending [16]. Therefore, constitutive modeling of the membrane and the bending response in a decoupled manner is necessary to accurately capture the forming behavior of CoFRTPs and predict the wrinkling behavior during forming [17–20].

Two-dimensional shell approaches achieve a membrane-bending decomposition by, for example, employing superimposed membrane and shell elements or specific out-of-plane integration schemes [20–23]. Initially, bending behavior was either neglected from consideration [24,25] or modeled purely elastic [20,26]. However, Dörr et al. [21,27] and Alshahrani and Hojjati [28] proved that the rate-dependent modeling of the bending behavior is crucial for the accurate prediction of the wrinkling behavior in the thermoforming process of CoFRTPs. Therefore, the rate-dependent nature of the material response is typically captured using viscoelastic models such as the Voigt-Kelvin model [20,21] or a generalized Maxwell approach [26,27].

Thermoforming of CoFRTPs is typically performed at elevated temperatures well above the crystallization temperature of the matrix material. During forming, convective cooling of the blank and contact with the colder mold can lower the temperature, significantly affecting the material behavior [29,30] and making the prediction of crystallization kinetics essential in thermoforming simulations [31]. Recent studies have implemented coupled thermomechanical approaches to capture temperature-dependent shear and bending behavior [26] and phase transitions between fluid and solid states within the thermoplastic material [22]. In particular, advances in thermomechanical modeling have emphasized the need for accurate prediction of temperature distribution through the thickness during thermoforming [32]. These works are based on the Alternate Direction Implicit (ADI) formulation [33], which effectively decomposes the thermal problem into a two-dimensional in-plane component and a one-dimensional through-thickness component. This approach enables 3D-like thermal modeling while maintaining computational efficiency through 2D mechanical shell elements making this approach particularly suitable for multi-layer simulation models [32]. Building upon a fully three-dimensional framework for through-thickness mechanical and thermal behavior, the fully coupled thermo-kinetic visco-hyperelastic constitutive model proposed by Bigot et al. [34] at the coupon scale could be extended in future work to simulate industrial-scale thermoforming processes of CoFRTPs.

1.2.2. 3D solid-shell elements

Despite significant advancements in thermoforming simulations for CoFRTPs, there remains a lack of simulation approaches capable of simultaneously capturing the compaction behavior of the material and predicting final part geometry. A finite element class which show promising results for the simulation of sheet metal forming are so-called solid-shell elements [35–37]. Solid-shell elements are a class of 3D finite elements that capture the behavior of thin-walled structures while avoiding the numerical locking issues (especially during bending deformation) associated with traditional solid elements. Unlike conventional shell elements, solid-shell elements allow for full 3D material modeling capabilities and therefore are a promising candidate to predict the compaction behavior within the simulation of the forming process for CoFRTPs. However, it is essential to note that these elements require a membrane-bending decomposition in order to accurately predict the wrinkling behavior during the forming process.

A large variety of solid-shell elements have been developed in the past, which are compared in detail by, e.g., Rah et al. [38], Schwarze and Reese [39], Schwarze and Reese [40], Mostafa [41]. The primary distinction among the various implementations of solid-shell elements pertains to their methods to avoid numerical locking based on the integration scheme, the number of collocation points for the *Assumed Natural Strain* (ANS)-method, and the number of *Enhanced Assumed Strain* (EAS) degrees of freedom (DOF). First implementations of solid-shell elements for implicit time-integration were initially proposed for the simulation of metal forming processes [42–44]. The formulation was later modified for explicit time-integration [45]. First proposals of solid-shell elements with a single integration point and three EAS-DOF were presented by Reese et al. [46] and Reese [47] which was later extended to variable number of integration points in thickness direction [48,49]. As reduced-integrated element formulations are numerically more efficient and less vulnerable to numerical locking phenomena, they are more suitable for the simulation of the forming process of CoFRTPs but need material-specific hourglass stabilization techniques.

1.2.3. Simulation approaches for the forming simulation of CoFRTPs employing 3D element formulations

An 8-node solid-shell element for the forming simulation of woven thermoplastic composites was proposed by Chen et al. [50,51]. The initial formulation demonstrates the capability to produce plausible results for shear angle distribution during the forming of complex geometries such as hemispherical and box-shaped parts [50]. In a follow-up study, the formulation was extended to include a viscoelastic material model and to investigate inter-ply slippage phenomena during the forming process [51]. However, no methods to consider a membrane-bending decomposition or to prevent numerical locking phenomena were proposed.

Xiong et al. [52,53] proposed a solid-shell element based on a 6-node prismatic element to model the consolidation of thermoplastic composite prepregs. The compaction behavior is incorporated through the implementation of an additional node in the element center, thereby enabling the prediction of pinching stresses. The solid-shell element utilizes a viscoelastic model based on a generalized Maxwell approach. The model incorporates an intimate contact model to describe the void reduction with time, pressure, and temperature. The model is able to accurately predict the compaction behavior within a thermoforming simulation of a double-dome geometry. The implementation necessitates a global DOF in contrast to an internal EAS-DOF, thereby constraining the implementation to specific solvers.

Dia et al. [54] proposed a nine-node hexahedral solid-shell element based on the geometry of a standard brick element. The formulation includes an additional node at the center of the element, equipped with a single degree of freedom in the thickness direction, enabling full 3D material modeling and improving the prediction of pinching stresses. To mitigate transverse shear locking, the element employs the ANS-method using a 4-node approach. The central degree of freedom is conceptually analogous to the enhancements introduced by the EAS method but offers enhanced accuracy in capturing through-thickness stress distributions compared to EAS-DOFs. This is because the EAS degrees of freedom do not significantly contribute to through-thickness stress prediction and are insufficient for accurately satisfying Neumann boundary conditions under transverse pressure loading, whereas the central node in Dia et al. [54] enables direct representation of

these stress components. No methods involving a membrane-bending decomposition were proposed.

Poppe et al. [55,56] implemented a built-in prismatic continuum shell element (SC6R) in combination with a user-defined element within Abaqus/Explicit (VUEL) to simulate the nonlinear compaction and simultaneous infiltration processes of wet compression molding. In order to capture the fabric's low bending stiffness, the model reduces the transverse shear stiffness rather than employing a full decoupling of the membrane and bending behavior. While this approach provides a reasonable approximation of the out-of-plane mechanical response, it inherently assumes an isotropic bending behavior with constant bending stiffness.

The solid-shell element formulation employed in this work is based on the Q1STs element formulation originally proposed by Schwarze and Reese [39,40], which features a reduced in-plane integration scheme, a four-point ANS-method, and a single EAS-DOF. This formulation was later adapted for explicit time integration by Pagani et al. [36], and its application was successfully demonstrated for the structural simulation of consolidated CoFRTPs [57,58]. However, its use in simulating the forming process of CoFRTPs was limited due to the absence of a membrane-bending decomposition [59]. To address this limitation, a further development of the Q1STs-based solid-shell element was introduced by Schäfer et al. [60,61] for the simulation of textile fabric forming processes. This enhanced formulation retains the key features while additionally enabling a membrane-bending decomposition. As a result, it allows for accurate predictions of wrinkling and realistic compaction behavior of textile fabrics during forming. However, the formulation currently does not support rate-dependent material models, thereby preventing its direct applicability to the thermoforming simulation of CoFRTPs.

The authors of the present work have previously proposed a 3D solid-shell element formulation for the thermoforming simulation of CoFRTPs [62,63]. This formulation builds upon the Q1STs element [39,40] and incorporates the modifications introduced by Schäfer et al. [60,61] to enable a membrane-bending decomposition. It was shown that the proposed formulation conceptually captures rate-dependent material behavior in numerical coupon tests using generic material parameters [62]. Building on this, a parameter study to assess the influence of material properties on the global deformation behavior during thermoforming simulation was conducted [63]. The findings indicated that parameters governing rate-dependency and bending behavior in the fiber direction exert a substantial influence on the global deformation behavior and must therefore be characterized precisely, whereas transverse shear properties have a minor impact on deformation and can be approximated within a reasonable order of magnitude to ensure numerical stability. Neither study included a comparison of the solid-shell formulation with experiments or an experimentally validated reference model to validate the global deformation behavior of the solid-shell element formulation. Also an evaluation of the resulting thickness distribution of the final part geometry was not performed.

1.3. Scope of this work and novel aspects

The objective of this study is to develop a 3D finite element formulation based on an 8-node hexahedral solid-shell element for the isothermal viscoelastic thermoforming simulation for CoFRTPs. The finite element is based on the Q1STs element formulation that was proposed by Schwarze and Reese [39,40] and was further developed by Schäfer et al. [60,61] to enable the simulation of the forming process of dry textile fabrics. The element formulation is implemented as a user-defined element VUEL for the commercial finite element software Abaqus. This work enhances the finite element formulation by newly incorporating a rate-dependent material behavior to predict the global deformation behavior during the thermoforming process for CoFRTPs. Additionally, a nonlinear compaction model is proposed and parameterized using experimental data from literature. To reduce the effort associated with material characterization for the solid-shell element, a new method for transferring of material properties from a 2D approach is investigated through a series of coupon-level simulations. The proposed 3D solid-shell element is validated by comparing the results of a single-layer CoFRTP thermoforming simulation against those obtained using an experimentally validated 2D approach, as a reference model. Finally, the thickness distribution of the final part geometry is evaluated to demonstrate the solid-shell element's capability to predict local thickness variations during the forming process.

2. Material modeling

2.1. Visco-hyperelastic membrane and bending modeling

To model the rate-dependent material behavior of the thermoplastic CoFRTPs, a visco-hyperelastic material model is employed. The visco-hyperelastic material model is applied in a decoupled manner for the in-plane membrane behavior and the bending behavior of the CoFRTPs. The membrane behavior is modeled using the Voigt-Kelvin approach and the *Ideal Fiber Reinforced Material* (IFRM) model [64,65]. The model ensures the quasi-inextensibility of the CoFRTPs in fiber direction through elevated elastic stiffnesses in that direction which is a common assumption for forming simulation of composites [19,21]. The bending behavior is modeled using the Voigt-Kelvin approach.

2.1.1. Voigt-Kelvin model

The Voigt-Kelvin model can be described as a parallel connection of a spring and a damper, wherein the spring represents the elastic behavior and the damper represents the viscous material response. Accordingly, the second Piola–Kirchhoff stress tensor $\boldsymbol{S}^{\mathrm{2PK}}$ is calculated by [66]

$$\boldsymbol{S}^{\mathrm{2PK}} = \boldsymbol{S}^{\mathrm{2PK}}_{\mathrm{elas}} + \boldsymbol{S}^{\mathrm{2PK}}_{\mathrm{visc}}, \tag{1}$$

comprising an elastic component $\boldsymbol{S}^{\mathrm{2PK}}_{\mathrm{elas}}$ and a viscous component $\boldsymbol{S}^{\mathrm{2PK}}_{\mathrm{visc}}$. The elastic stress component $\boldsymbol{S}^{\mathrm{2PK}}_{\mathrm{elas}}$ is connected to a strain energy $W = 1/2\ \boldsymbol{E} \cdot \mathbb{C}[\boldsymbol{E}]$ and can be calculated using the hyperelastic St. Venant-Kirchhoff model [67]

$$\boldsymbol{S}^{\mathrm{2PK}}_{\mathrm{elas}} = \mathbb{C}[\boldsymbol{E}], \tag{2}$$

where $\mathbb{C}$ represents the stiffness tensor, while $\boldsymbol{E}$ denotes the Green–Lagrange strain tensor. Due to the dominant in-plane characteristics of CoFRTPs, the stiffness tensor $\mathbb{C}$ is typically highly anisotropic, characterized by a high stiffness along the fiber direction and significantly lower stiffnesses in both the transverse and shear directions.

The viscous part of the Voigt-Kelvin approach (Eq. (1)) is modeled utilizing an isotropic Newton model [68]

$$\boldsymbol{\sigma}_{\mathrm{visc}} = \eta \boldsymbol{D}, \tag{3}$$

where the viscous Cauchy stress $\boldsymbol{\sigma}_{\mathrm{visc}}$ is calculated using the viscosity η and the deformation rate tensor $\boldsymbol{D}$. In this work, the viscosity η (Eq. (3)) is modeled using the Cross model, which defines the viscosity as a function of the scalar deformation rate $\dot{\gamma}$ [68]

$$\eta(\dot{\gamma}) = \frac{\eta_0 - \eta_\infty}{1 + m\dot{\gamma}^{(1-n)}}\eta_\infty. \tag{4}$$

In Eq. (4), η_0 is the zero shear viscosity, η_∞ the infinite shear viscosity, and m and n are Cross model parameters. The deformation rate $\dot{\gamma}$ is the Frobenius norm of $\boldsymbol{D}$

$$\dot{\gamma} = \sqrt{2\boldsymbol{D} \cdot \boldsymbol{D}}. \tag{5}$$

Using the rate of the Green–Lagrange strain tensor $\dot{\boldsymbol{E}}$ [66], $\boldsymbol{D}$ can be calculated

$$\boldsymbol{D} = \boldsymbol{F}^{-\mathrm{T}}\dot{\boldsymbol{E}}\boldsymbol{F}^{-1}. \tag{6}$$

To evaluate Eq. (1) in the initial configuration, the viscous Cauchy stress $\boldsymbol{\sigma}_{\mathrm{visc}}$ is transformed to the second Piola–Kirchhoff stress tensor

$\boldsymbol{S}^{\mathrm{2PK}}_{\mathrm{visc}}$ using the deformation gradient tensor $\boldsymbol{F}$ and its determinant $J = \det(\boldsymbol{F})$

$$\boldsymbol{S}^{\mathrm{2PK}}_{\mathrm{visc}} = J\boldsymbol{F}^{-1}\boldsymbol{\sigma}_{\mathrm{visc}}\boldsymbol{F}^{-\mathsf{T}}. \tag{7}$$

Note, that the Voigt-Kelvin approach (Eq. (1)) is a comparably simple model for the rate-dependent membrane and bending behavior of CoFRTPs. More sophisticated multi-mode formulations, such as generalized Maxwell models with Prony-series relaxation (e.g., [26,27]), can represent a broader range of relaxation times and long-term viscous effects and can model the viscoelastic behavior more realistically. However, in the present work, the Voigt-Kelvin approach is chosen for its simplicity and computational efficiency.

2.2. Nonlinear compaction behavior

The experimental investigations in the literature demonstrate that the compaction behavior of CoFRTPs is nonlinear and follows an exponential progression for rising compaction displacements [53,69]. To model the nonlinear compaction behavior of CoFRTPs, the compaction stiffness C_{C} is modeled as an exponential function of the compaction strain E_{33}. Therefore, the following approach is employed

$$C_{\mathrm{C}}\left(E_{33}\right) = a \cdot \exp\left(-c \cdot E_{33}\right), \tag{8}$$

where a and c are fitting parameters.

To identify the parameters a and c, the deformation is assumed purely compressive, i.e., without consideration of Poisson's ratios. The deformation gradient $\boldsymbol{F}_{\mathrm{C}}$, which describes the deformation state, can be expressed as

$$\boldsymbol{F}_{\mathrm{C}} = \begin{bmatrix} 1 & 0 & 0 \\ 0 & 1 & 0 \\ 0 & 0 & \lambda_z \end{bmatrix} \boldsymbol{e}_i \otimes \boldsymbol{e}_j \text{ with } \lambda_z = \frac{t - u_{\mathrm{C}}}{t}. \tag{9}$$

Here, $\lambda_z \in [0, 1]$ describes the relative thickness deviation of the CoFRTP with the initial thickness t and the compaction displacement u_{C}. The corresponding Green–Lagrange strain tensor $\boldsymbol{E}$ can be obtained by

$$\boldsymbol{E} = \frac{1}{2}\left(\boldsymbol{F}_{\mathrm{C}}^{\mathsf{T}}\boldsymbol{F}_{\mathrm{C}} - \boldsymbol{I}\right). \tag{10}$$

In a subsequent evaluation step, the experimentally measured compaction force R_{C} is used to calculate the corresponding second Piola–Kirchhoff stress tensor $\boldsymbol{S}^{\mathrm{2PK}}$. For this the first Piola–Kirchhoff stress tensor $\boldsymbol{S}^{\mathrm{1PK}}$ is computed using the initial cross-sectional area A and the measured compaction force R_{C}

$$\boldsymbol{S}^{\mathrm{1PK}} = \frac{R_{\mathrm{C}}}{A}\boldsymbol{e}_3 \otimes \boldsymbol{e}_3. \tag{11}$$

The second Piola–Kirchhoff stress tensor $\boldsymbol{S}^{\mathrm{2PK}}$ can be calculated using the deformation gradient $\boldsymbol{F}_{\mathrm{C}}$

$$\boldsymbol{S}^{\mathrm{2PK}} = \boldsymbol{F}_{\mathrm{C}}^{-1}\boldsymbol{S}^{\mathrm{1PK}}. \tag{12}$$

Finally, by combining the kinematic assumption (Eq. (9)) with the kinematic identities (Eqs. (10), (11) and (12)) and the constitutive model (Eqs. (2), (8)), the fitting parameters a and c can be determined.

3. Element formulations

3.1. Two-dimensional approach

3.1.1. Implementation in Abaqus/Explicit using superimposed two-dimensional elements

In this study, an experimentally validated methodology for macroscopic thermoforming simulation of CoFRTPs using a 2D approach, utilizing a decomposition of membrane and bending behavior is employed for comparison. The approach is implemented in the commercial finite element software Abaqus/Explicit and is based on the work of Dörr et al. [21].

To decompose membrane and bending behavior, separate membrane and plate (bending) elements are superimposed at shared nodes. This strategy allows for the independent computation of in-plane forces $\boldsymbol{N}$ and bending moments $\boldsymbol{M}$ within the respective elements, enabling a decomposed and consistent representation of in-plane membrane and out-of-plane bending material responses in a unified finite element formulation. The membrane's behavior is described using membrane elements (M3D3) and a VUMAT subroutine. The bending behavior is modeled using shell elements (S3) and a VUGENS subroutine which computes the bending moments $\boldsymbol{M}$ from the incremental curvature tensors $\Delta\boldsymbol{\kappa}$ at the shell mid-face. The material models for both the membrane and bending behavior are based on the Voigt-Kelvin approach from Section 2.1.1.

3.1.2. Parameters of the 2D material model

As this work investigates the correspondence of material parameters using different element formulations, a brief overview of the material parameters used in the 2D approach is provided in the following.

Two distinct elastic stiffness tensors, $\mathbb{C}^{\mathrm{2D,M}}$ and $\mathbb{C}^{\mathrm{2D,B}}$, are defined for the elastic membrane and bending behavior. The elastic law for the membrane in 2D Voigt-notation reads (cf. Eq. (2))

$$\underbrace{\begin{bmatrix} E_{\mathrm{F}}^{\mathrm{2D,M}} + E_{\mathrm{M}}^{\mathrm{2D,M}} & 0 & 0 \\ 0 & E_{\mathrm{M}}^{\mathrm{2D,M}} & 0 \\ 0 & 0 & G_{\mathrm{M}}^{\mathrm{2D,M}} \end{bmatrix}}_{\widehat{=}\mathbb{C}^{\mathrm{2D,M}}} \underbrace{\begin{bmatrix} E_{11}^{\mathrm{2D,M}} \\ E_{22}^{\mathrm{2D,M}} \\ 2E_{12}^{\mathrm{2D,M}} \end{bmatrix}}_{\widehat{=}\boldsymbol{E}^{\mathrm{2D,M}}} = \underbrace{\begin{bmatrix} S_{11}^{\mathrm{2D,M}} \\ S_{22}^{\mathrm{2D,M}} \\ S_{12}^{\mathrm{2D,M}} \end{bmatrix}}_{\widehat{=}\boldsymbol{S}_{\mathrm{elast}}^{\mathrm{2D,M}}}. \tag{13}$$

The Youngs Moduli $E_{\mathrm{F}}^{\mathrm{2D,M}}$ represent the stiffness in fiber direction. The modulus $E_{\mathrm{M}}^{\mathrm{2D,M}}$ describes the isotropic stiffness of the matrix, which is typically several orders of magnitude lower than the stiffness along the fiber direction. The in-plane Possion ratio $\nu_{12}^{\mathrm{2D,M}}$ is assumed to be negligible due to the high contrast between the in-plane stiffnesses. Consequently, the in-plane shear modulus $G_{\mathrm{M}}^{\mathrm{2D,M}}$ can be calculated using

$$G_{\mathrm{M}}^{\mathrm{2D,M}} = \frac{E_{\mathrm{M}}^{\mathrm{2D,M}}}{2\left(1 + \nu_{12}^{\mathrm{2D,M}}\right)} = \frac{E_{\mathrm{M}}^{\mathrm{2D,M}}}{2}. \tag{14}$$

The elastic law for the bending in 2D Voigt-notation reads (cf. Eq. (2))

$$\underbrace{\begin{bmatrix} C_{11}^{\mathrm{2D,B}} & 0 & 0 \\ 0 & C_{22}^{\mathrm{2D,B}} & 0 \\ 0 & 0 & C_{12}^{\mathrm{2D,B}} \end{bmatrix}}_{\widehat{=}\mathbb{C}^{\mathrm{2D,B}}} \underbrace{\begin{bmatrix} \varepsilon_{11}^{\mathrm{2D,B}} \\ \varepsilon_{22}^{\mathrm{2D,B}} \\ 2\varepsilon_{12}^{\mathrm{2D,B}} \end{bmatrix}}_{\widehat{=}\boldsymbol{\varepsilon}^{\mathrm{2D,B}}} = \underbrace{\begin{bmatrix} \sigma_{11}^{\mathrm{2D,B}} \\ \sigma_{22}^{\mathrm{2D,B}} \\ \sigma_{12}^{\mathrm{2D,B}} \end{bmatrix}}_{\widehat{=}\boldsymbol{\sigma}_{\mathrm{elast}}^{\mathrm{2D,B}}}. \tag{15}$$

The bending stiffnesses $C_{11}^{\mathrm{2D,B}}$ and $C_{22}^{\mathrm{2D,B}}$ describe the stiffnesses in fiber direction and perpendicular to the fiber direction, respectively. The bending stiffness $C_{12}^{\mathrm{2D,B}}$ characterizes the bending resistance along the direction diagonal to the material's principal axes. Note that the 2D approach uses infinitesimal strain theory, as the strain tensor $\boldsymbol{\varepsilon}$ is approximated in the VUGENS subroutine [21].

The viscous behavior within the 2D approach follows an isotropic Newton model (Eq. (3)) extended by a Cross viscosity law (Eq. (4)). The rate-dependent approach is applied separately for the membrane and bending behavior. Therefore, the viscous material parameters η_0^{2D}, $\eta_\infty^{\mathrm{2D}}$, m^{2D}, and n^{2D} are required for both the membrane and bending behavior.

3.2. Solid-shell element

3.2.1. Fundamental element formulation

The 3D hexahedral solid-shell element utilized in this study is based on the Q1STs element originally proposed by Schwarze and Reese [39,40] and was extended to an explicit formulation by Pagani et al.

[36]. An exhaustive derivation of the element formulation can be found in the original publications. A concise overview of the major features of the solid-shell element used is given below.

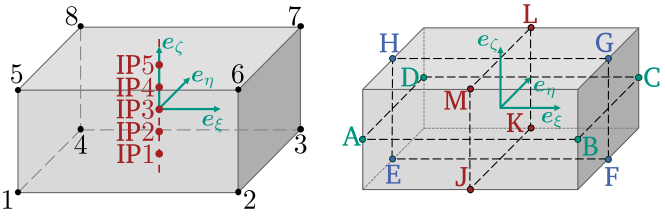

(a) Geometry of the solid-shell element

(b) Collocation points for the ANS method

Fig. 1. Isoparametric solid-shell element (based on [35,39,40]).

The geometry of the used solid-shell element utilized is a standard 8-node hexahedral finite element with only translational degrees of freedom, cf. Fig. 1(a). For the interpolation of the displacements within the element, tri-linear shape functions are employed. These shape functions are defined in the natural coordinates $\boldsymbol{\xi} \hat{=} (\xi, \eta, \zeta)^\top$ of the element [67]

$$N_I = \frac{1}{8}(1 + \xi\xi_I)(1 + \eta\eta_I)(1 + \zeta\zeta_I), \quad I = 1, \dots, 8. \tag{16}$$

Here, $\boldsymbol{\xi}_I$ are the natural coordinates of the nodes of the element. In order to carry out the numerical integration of the weak form, a reduced integration scheme is utilized in the in-plane direction, and a full integration is employed in the thickness direction. The full integration in thickness direction is performed using a standard Gauss–Legendre quadrature with a variable number of integration points. The integration points are stacked in the middle plane of the element in thickness direction and their locations are given by $\boldsymbol{\xi}^\star = \zeta^\star \boldsymbol{e}_\zeta$ (cf. Fig. 1(a)). Note, that the natural coordinates of the integration points $\zeta^\star$ and the corresponding weights for the numerical integration depend on the selected number of integration points.

In order to prevent numerical locking phenomena, a variety of computational techniques are employed, modifying the strain $\boldsymbol{E}$ in the solid-shell element. The strain tensor $\boldsymbol{E}$ in natural coordinates $\boldsymbol{\xi}$ reads

$$\boldsymbol{E} = \begin{bmatrix} E_{\xi\xi} & E_{\xi\eta} & E_{\xi\zeta} \\ E_{\eta\xi} & E_{\eta\eta} & E_{\eta\zeta} \\ E_{\zeta\xi} & E_{\zeta\eta} & E_{\zeta\zeta} \end{bmatrix} \boldsymbol{e}_i \otimes \boldsymbol{e}_j \text{ with } i, j \in \{\xi, \eta, \zeta\}. \tag{17}$$

The EAS-method [70–72] is the first technique employed to avoid numerical locking. This method involves the decomposition of the total strain tensor $\boldsymbol{E}$ into a compatible part $\boldsymbol{E}_\mathrm{C}$ and an enhanced part $\boldsymbol{E}_\mathrm{e}$

$$\boldsymbol{E} = \boldsymbol{E}_\mathrm{C}(\boldsymbol{u}_I) + \boldsymbol{E}_\mathrm{e}. \tag{18}$$

The compatible strain $\boldsymbol{E}_\mathrm{C}$ is exclusively dependent on the node displacements $\boldsymbol{u}_I$ while $\boldsymbol{E}_\mathrm{e}$ covers deformation modes incompatible with the linear shape functions. Consequently, the corresponding weak forms for explicit time integration schemes read [36]

$$g_1(\boldsymbol{u}, \boldsymbol{E}_\mathrm{e}) = \int_{V_0} \boldsymbol{S}(\boldsymbol{E}) \cdot \delta\boldsymbol{E}_\mathrm{C} \, \mathrm{d}V + \int_{V_0} \rho_0 \ddot{\boldsymbol{u}} \cdot \delta\boldsymbol{u} \, \mathrm{d}V + g_\mathrm{ext} = 0; \tag{19}$$

$$g_2(\boldsymbol{u}, \boldsymbol{E}_\mathrm{e}) = \int_{V_0} \boldsymbol{S}(\boldsymbol{E}) \cdot \delta\boldsymbol{E}_\mathrm{e} \, \mathrm{d}V = 0; \tag{20}$$

where $\boldsymbol{S}$ is the second Piola–Kirchhoff stress tensor, ρ_0 is the material density, $\boldsymbol{u}$ is the displacement field and g_ext is the external work. In the present work, the enhanced strain $\boldsymbol{E}_\mathrm{e}$ is introduced as

$$\boldsymbol{E}_\mathrm{e} = \alpha_\mathrm{e} \boldsymbol{B}_\mathrm{e} \quad \text{with} \quad \boldsymbol{B}_\mathrm{e} = \zeta \boldsymbol{e}_\zeta \otimes \boldsymbol{e}_\zeta, \tag{21}$$

where α_e is an enhanced degree of freedom (EAS-DOF). The EAS concept has been demonstrated to facilitate the avoidance of volumetric locking phenomena and maintain optimal performance for nearly incompressible materials in problems dominated by bending [72]. The approach in Eq. (21) was introduced by Schwarze and Reese [40] and was verified by Pagani et al. [36] for the explicit formulation. A comprehensive overview of the discretization and the integration of the weak form within the utilized solid-shell element can be found in Pagani et al. [36].

The second technique to prevent locking phenomena is the so-called ANS-method, which was first proposed by Bathe and Dvorkin [73]. The evaluation is based on a reinterpolation of shear terms from assumed shear locking-free collocation points, which are located on the elements' edges (cf. Fig. 1(b)). The values of these shear terms are then interpolated within the reference element. This approach has been demonstrated to circumvent both transversal shear locking and curvature thickness locking [35,74]. The transverse normal strain $E_{\mathrm{c},\zeta\zeta}$ is modified to avoid curvature thickness locking [75,76].

$$E_{\mathrm{c},\zeta\zeta}(\xi, \eta) = \sum_{P_{\zeta\zeta}=\mathrm{A}}^{\mathrm{D}} \frac{1}{4} \left(1 + \xi_{P_{\zeta\zeta}} \xi\right) \left(1 + \eta_{P_{\zeta\zeta}} \eta\right) E_{\mathrm{c},\zeta\zeta}(\boldsymbol{\xi}_{P_{\zeta\zeta}}). \tag{22}$$

The utilized collocation points $P_{\zeta\zeta} = \{A, B, C, D\}$ are located on the edges of the $(\boldsymbol{e}_\xi, \boldsymbol{e}_\eta)$-plane of the element (cf. Fig. 1(b)). The strain components $E_{\mathrm{c},\eta\zeta}$ and $E_{\mathrm{c},\xi\zeta}$ are modified to avoid transveral shear locking [35,73]

$$E_{\mathrm{c},\eta\zeta}(\xi, \zeta) = \sum_{P_{\eta\zeta}=\mathrm{E}}^{\mathrm{H}} \frac{1}{4} \left(1 + \xi_{P_{\eta\zeta}} \xi\right) \left(1 + \zeta_{P_{\eta\zeta}} \zeta\right) E_{\mathrm{c},\eta\zeta}(\boldsymbol{\xi}_{P_{\eta\zeta}}) \tag{23}$$

$$E_{\mathrm{c},\xi\zeta}(\eta, \zeta) = \sum_{P_{\xi\zeta}=\mathrm{J}}^{\mathrm{M}} \frac{1}{4} \left(1 + \eta_{P_{\xi\zeta}} \eta\right) \left(1 + \zeta_{P_{\xi\zeta}} \zeta\right) E_{\mathrm{c},\xi\zeta}(\boldsymbol{\xi}_{P_{\xi\zeta}}). \tag{24}$$

The utilized collocation points $P_{\eta\zeta} = \{E, F, G, H\}$ and $P_{\xi\zeta} = \{J, K, L, M\}$ are located on the edges of the $(\boldsymbol{e}_\xi, \boldsymbol{e}_\zeta)$-plane and $(\boldsymbol{e}_\eta, \boldsymbol{e}_\zeta)$-plane of the element, respectively (cf. Fig. 1(b)).

All integration points of the solid-shell element are situated in the normal trough the element center $\boldsymbol{\xi}^\star = \zeta^\star \boldsymbol{e}_\zeta$ [77]. Therefore, the compatible strain $\boldsymbol{E}_\mathrm{C}$ can be split into a part, which is related to the strains at the integration points $\boldsymbol{E}_\mathrm{C}^\star = \boldsymbol{E}_\mathrm{C}(\boldsymbol{\xi}^\star)$ and a part called hourglass strain $\boldsymbol{E}_\mathrm{C}^\mathrm{hg}$ [40]

$$\boldsymbol{E}_\mathrm{C} = \boldsymbol{E}_\mathrm{C}^\star + \boldsymbol{E}_\mathrm{C}^\mathrm{hg}. \tag{25}$$

The compatible strain $\boldsymbol{E}_\mathrm{C}^\star$ in Eq. (25) is used to evaluate the constitutive material law at the integration points. The hourglass strain $\boldsymbol{E}_\mathrm{C}^\mathrm{hg}$ is employed to ensure the full rank of the element formulation and is therefore relevant for the numerical stability of the element. To calculate the two parts of the compatible strain $\boldsymbol{E}_\mathrm{C}$, it is expanded in a Taylor series around the element center $\boldsymbol{\xi}^0 = \boldsymbol{0}$ [40]

$$\boldsymbol{E}_\mathrm{C} = \underbrace{\boldsymbol{E}_\mathrm{C}^0 + \zeta \boldsymbol{E}_\mathrm{C}^\zeta + \zeta^2 \boldsymbol{E}_\mathrm{C}^{\zeta\zeta}}_{\boldsymbol{E}_\mathrm{C}^\star} + \underbrace{\xi \boldsymbol{E}_\mathrm{C}^\xi + \eta \boldsymbol{E}_\mathrm{C}^\eta + \xi\eta \boldsymbol{E}_\mathrm{C}^{\xi\eta} + \xi\zeta \boldsymbol{E}_\mathrm{C}^{\xi\zeta} + \eta\zeta \boldsymbol{E}_\mathrm{C}^{\eta\zeta}}_{\boldsymbol{E}_\mathrm{C}^\mathrm{hg}}$$

$$\text{with} \quad \boldsymbol{E}_\mathrm{C}^{\xi_i} = \left(\frac{\partial \boldsymbol{E}_\mathrm{C}}{\partial \xi_i} \right)_{\xi = \xi^0}. \tag{26}$$

The tensor-valued derivatives $\boldsymbol{E}_\mathrm{C}^{\xi_i}$ are explicitly given, e.g., by Schwarze and Reese [40]. Note, that the strain $\boldsymbol{E}_\mathrm{C}^\star$ in Eq. (26) is quadratic in ζ which was found to be more accurate than a linear approximation [40].

Analogous, a Taylor expansion with respect to the element center $\boldsymbol{\xi}^0 = \boldsymbol{0}$ is applied on the second Piola–Kirchhoff stress $\boldsymbol{S}$ which can be expressed as [40,47]

$$\boldsymbol{S} = \underbrace{\boldsymbol{S}\left(\boldsymbol{E}^\star\right)}_{\boldsymbol{S}^\star} + \underbrace{\overbrace{\left(\frac{\partial \boldsymbol{S}(\boldsymbol{E})}{\partial \boldsymbol{E}} \right)_{\xi = \xi^0}}^{\mathbb{C}^\star} \left[\xi \boldsymbol{E}_\mathrm{C}^\xi + \eta \boldsymbol{E}_\mathrm{C}^\eta + \xi\zeta \boldsymbol{E}_\mathrm{C}^{\xi\zeta} + \eta\zeta \boldsymbol{E}_\mathrm{C}^{\eta\zeta} \right]}_{\boldsymbol{S}^\mathrm{hg}}. \tag{27}$$

The term $\boldsymbol{S}^\star$ represents the stresses, which are evaluated at the integration points $\boldsymbol{\xi}^\star$. The term $\boldsymbol{S}^\mathrm{hg}$ represents the hourglass stresses. Note, that the stiffness tangent $\mathbb{C}^\star$ at the element center $\boldsymbol{\xi}^0$ can be material-

and deformation-dependent. To enable and analytical integration of the hourglass stresses, the stiffness tangent $\mathbb{C}^{\star}$ is approximated by a constant stiffness tensor $\mathbb{C}^{\mathrm{hg}}$ [60].

For a more thorough exposition of the fundamental formulation of the solid-shell element and its implementation, the reader is directed to the original publications [36,39,40].

3.2.2. Membrane-bending decomposition

In order to accurately simulate the forming process of CoFRTPs, the presented solid-shell element requires a membrane-bending decomposition similar to the one used in the 2D approach. The methodology to achieve this decomposition is based on the work of Schäfer et al. [60,61] and is briefly outlined in the following.

The total strain $\boldsymbol{E}$ is decomposed into a part that is constant over the thickness of the solid-shell element, the membrane strain $\boldsymbol{E}^{\mathrm{M}}$, and a part that varies over the thickness of the solid-shell element, the bending strain $\boldsymbol{E}^{\mathrm{B}}$,

$$\boldsymbol{E} = \boldsymbol{E}_{\mathrm{e}} + \boldsymbol{E}_{\mathrm{C}} = \overbrace{\underbrace{\boldsymbol{E}_{\mathrm{e}} + \boldsymbol{E}_{\mathrm{C}}^{0}}_{\boldsymbol{E}^{\mathrm{M}}} + \underbrace{\zeta \boldsymbol{E}_{\mathrm{C}}^{\zeta} + \zeta^{2} \boldsymbol{E}_{\mathrm{C}}^{\zeta\zeta}}_{\boldsymbol{E}^{\mathrm{B}}}}^{\boldsymbol{E}^{\star}} + \boldsymbol{E}_{\mathrm{C}}^{\mathrm{hg}}. \tag{28}$$

To decompose membrane and bending deformation modes, the stresses relevant for the integration scheme of the solid-shell element $\boldsymbol{S}^{\star}$ are decomposed into a part that is constant over the thickness of the solid-shell element, the membrane stress $\boldsymbol{S}^{\mathrm{M}}$, and a part that varies over the thickness of the solid-shell element, the bending stress $\boldsymbol{S}^{\mathrm{B}}$. Consequently, the total stress $\boldsymbol{S}$ can be expressed as [60,61,78]

$$\boldsymbol{S} = \underbrace{\boldsymbol{S}^{\mathrm{M}}\left(\boldsymbol{E}^{\mathrm{M}}\right) + \boldsymbol{S}^{\mathrm{B}}\left(\boldsymbol{E}^{\mathrm{B}}\right)}_{\boldsymbol{S}^{\star}} + \boldsymbol{S}^{\mathrm{hg}}\left(\boldsymbol{E}^{\mathrm{hg}}\right) = \mathbb{C}^{\mathrm{M}}\left[\boldsymbol{E}^{\mathrm{M}}\right] + \mathbb{C}^{\mathrm{B}}\left[\boldsymbol{E}^{\mathrm{B}}\right] + \mathbb{C}^{\mathrm{hg}}\left[\boldsymbol{E}_{\mathrm{C}}^{\mathrm{hg}}\right]. \tag{29}$$

As demonstrated by Schäfer et al. [60], the decomposition method outlined in Eq. (29) enables the isolation of the material response into membrane and bending deformation modes. For the hourglass stabilization, the hourglass stiffness

$$\left(\frac{\partial \boldsymbol{S}}{\partial \boldsymbol{E}}\right)_{\xi=\xi^{0}} = \mathbb{C}^{\mathrm{hg}} = \mathbb{C}^{\mathrm{M}} \tag{30}$$

proved to be a suitable approximation for highly anisotropic engineering textiles [60].

3.2.3. Enabling rate-dependent material behavior

In order to implement the Voigt-Kelvin approach, cf. Section 2.1.1, in the solid-shell element and enable rate-dependent material modeling, different enhancements are necessary. First, the viscous stresses in Eq. (3) are a function of $\boldsymbol{D}$. The deformation rate tensor $\boldsymbol{D}$ can be calculated from the strain rate tensor $\dot{\boldsymbol{E}}$ and the deformation gradient $\boldsymbol{F}$ using Eq. (6). However, the deformation gradient $\boldsymbol{F}$, is not directly available in the solid-shell element due to the modifications of the Green–Lagrange strain $\boldsymbol{E}$ based on the EAS- and ANS-method (cf. Section 3.2.1). Consequently, the Green–Lagrange strain tensor $\boldsymbol{E}$, derived from Eq. (28), does not generally describe the same deformation state as the strain tensor that solely results from the tri-linear shape functions (Eq. (16)) and the nodes' displacements $\boldsymbol{u}_I$. Therefore, an appropriate approximation $\boldsymbol{F}_{\mathrm{tec}}$ for $\boldsymbol{F}$ in dependence on a modified strain tensor $\boldsymbol{E}_{\mathrm{mod}}$ is required.

Hauptmann et al. [43] and Mitsch et al. [62] proposed a routine for a suitable approximation $\boldsymbol{F}_{\mathrm{tec}}$ in dependence on modified strain measurements $\boldsymbol{E}_{\mathrm{mod}}$. To this end, the polar decomposition for the deformation gradient $\boldsymbol{F}_{\mathrm{tec}}$ is employed [66]

$$\boldsymbol{F}_{\mathrm{tec}} = \boldsymbol{R}\boldsymbol{U}_{\mathrm{tec}}. \tag{31}$$

The symmetric second-order tensor $\boldsymbol{U}_{\mathrm{tec}}$ is referred to as the stretch tensor and can be calculated from a modified Green–Lagrange strain tensor $\boldsymbol{E}_{\mathrm{mod}}$ using

$$\left(\boldsymbol{U}_{\mathrm{tec}}\right)^{2} = 2\boldsymbol{E}_{\mathrm{mod}} + \boldsymbol{I} \tag{32}$$

where $\boldsymbol{I}$ is the second-order identity tensor. The orthogonal second-order tensor $\boldsymbol{R}$ in Eq. (31) describes the rigid body rotation in $\boldsymbol{F}_{\mathrm{tec}}$ and is calculated using the polar decomposition of the deformation gradient $\boldsymbol{F}$ which corresponds to the original node displacements $\boldsymbol{u}_I$. Subsequently, the approximated deformation gradient $\boldsymbol{F}_{\mathrm{tec}}$ can be calculated (Eq. (31)). It is then used to calculate the viscous Cauchy stress tensor $\boldsymbol{\sigma}^{\mathrm{visc}}$ (Eq. (3)) and the corresponding second Piola–Kirchhoff stress tensor $\boldsymbol{S}^{\mathrm{visc}}$ (Eq. (7)). Finally, the rate-dependent material behavior of the solid-shell element can be applied as constitutive equations for the membrane and the bending behavior. The corresponding stress reads

$$\boldsymbol{S} = \underbrace{\boldsymbol{S}_{\mathrm{M}}\left(\boldsymbol{E}_{\mathrm{M}}, \dot{\boldsymbol{E}}_{\mathrm{M}}\right) + \boldsymbol{S}_{\mathrm{B}}\left(\boldsymbol{E}_{\mathrm{B}}, \dot{\boldsymbol{E}}_{\mathrm{B}}\right)}_{\boldsymbol{S}^{\star}} + \boldsymbol{S}^{\mathrm{hg}}. \tag{33}$$

As demonstrated by Mitsch et al. [62], this approach enables the description of the rate-dependent material behavior of the solid-shell element, while ensuring the preservation of membrane-bending decomposition.

With the introduction of rate-dependency, the Taylor expansion of the total stress $\boldsymbol{S}(\boldsymbol{E}, \dot{\boldsymbol{E}})$ around the element center $\boldsymbol{\xi}^{0}$ (cf. Eq. (27)) now includes derivatives with respect to both the strain $\boldsymbol{E}$ and the strain rate $\dot{\boldsymbol{E}}$. Therefore, the hourglass stress $\boldsymbol{S}^{\mathrm{hg}}$ is no longer solely dependent on the strain $\boldsymbol{E}$, but also on the strain rate $\dot{\boldsymbol{E}}$. In earlier work on anisotropic elasticity [60,61], the hourglass stabilization was based on the material tangent evaluated in the mid-plane of the element, which proved effective for the purely elastic case (cf. Eq. (30)). The concept to use the material's resistance against deformation in the mid-plane of the element $\boldsymbol{\xi}^{0}$ to calculate the hourglass stress is now extended to the rate-dependent case. Specifically, the material tangent with respect to the strain rate $\dot{\boldsymbol{E}}$ is used to represent the viscous contribution in the hourglass stabilization. The contribution of rate-dependent hourglass stress $\boldsymbol{S}_{\mathrm{visc}}^{\mathrm{hg}}$ to the total stress can be considered by decomposing the hourglass stress $\boldsymbol{S}^{\mathrm{hg}}$ into an elastic part $\boldsymbol{S}_{\mathrm{elast}}^{\mathrm{hg}}$ and a viscous part $\boldsymbol{S}_{\mathrm{visc}}^{\mathrm{hg}}$ using the Voigt-Kelvin approach (Eq. (1)),

$$\boldsymbol{S}^{\mathrm{hg}} = \overbrace{\underbrace{\left(\frac{\partial \boldsymbol{S}_{\mathrm{elast}}(\boldsymbol{E})}{\partial \boldsymbol{E}}\right)_{\xi=\xi^{0}}}_{\mathbb{C}^{\star}}\left[\boldsymbol{E}_{\mathrm{C}}^{\mathrm{hg}}\right]}^{\boldsymbol{S}_{\mathrm{elast}}^{\mathrm{hg}}} + \overbrace{\underbrace{\left(\frac{\partial \boldsymbol{S}_{\mathrm{visc}}(\dot{\boldsymbol{E}})}{\partial \dot{\boldsymbol{E}}}\right)_{\xi=\xi^{0}}}_{\mathbb{V}^{\star}}\left[\dot{\boldsymbol{E}}_{\mathrm{C}}^{\mathrm{hg}}\right]}^{\boldsymbol{S}_{\mathrm{visc}}^{\mathrm{hg}}}. \tag{34}$$

The tensor $\mathbb{V}^{\star}$ in Eq. (34) represents the hourglass viscosity tensor, which serves as the viscous counterpart to the hourglass stiffness tensor $\mathbb{C}^{\star}$. The derivation of the hourglass viscosity tensor $\mathbb{V}^{\star}$ is described in detail in Appendix A. The viscous hourglass stresses $\boldsymbol{S}_{\mathrm{visc}}^{\mathrm{hg}}$ are calculated using Eq. (A.8)

$$\begin{aligned}\boldsymbol{S}_{\mathrm{visc}}^{\mathrm{hg}} &= \mathbb{V}^{\star}\left[\dot{\boldsymbol{E}}_{\mathrm{C}}^{\mathrm{hg}}\right] = \mathbb{V}^{\star}\left[\xi\dot{\boldsymbol{E}}_{\mathrm{C}}^{\xi} + \eta\dot{\boldsymbol{E}}_{\mathrm{C}}^{\eta} + \xi\eta\dot{\boldsymbol{E}}_{\mathrm{C}}^{\xi\eta} + \xi\zeta\dot{\boldsymbol{E}}_{\mathrm{C}}^{\xi\zeta} + \eta\zeta\dot{\boldsymbol{E}}_{\mathrm{C}}^{\eta\zeta}\right] \\ &= J\eta^{\mathrm{M}}\boldsymbol{C}^{-1}\left(\xi\dot{\boldsymbol{E}}_{\mathrm{C}}^{\xi} + \eta\dot{\boldsymbol{E}}_{\mathrm{C}}^{\eta} + \xi\eta\dot{\boldsymbol{E}}_{\mathrm{C}}^{\xi\eta} + \xi\zeta\dot{\boldsymbol{E}}_{\mathrm{C}}^{\xi\zeta} + \eta\zeta\dot{\boldsymbol{E}}_{\mathrm{C}}^{\eta\zeta}\right)\boldsymbol{C}^{-1},\end{aligned} \tag{35}$$

where η^{M} is the material's viscosity in the mid-plane $\boldsymbol{\xi} = \boldsymbol{0}$ of the solid-shell element. The tensor $\boldsymbol{C} = \boldsymbol{F}^{\mathrm{T}}\boldsymbol{F}$ is the right Cauchy–Green tensor which was obtained using $\boldsymbol{F}_{\mathrm{tec}}$ from Eq. (31) and J is the determinant of $\boldsymbol{F}_{\mathrm{tec}}$.

3.2.4. Parameters of the 3D material model

As this work investigates the correspondence of material parameters using different element formulations, a brief summary of the material parameters utilized in the solid-shell element is provided in the following.

Two elastic stiffness tensors $\mathbb{C}^{3D,M}$ and $\mathbb{C}^{3D,B}$ are defined for the elastic membrane and bending behavior. The elastic law for the membrane behavior in Voigt-notation reads (cf. Eq. (2))

$$\underbrace{\begin{bmatrix} C_{11}^{3D,M} & 0 & 0 & 0 & 0 & 0 \\ 0 & C_{22}^{3D,M} & 0 & 0 & 0 & 0 \\ 0 & 0 & C_{33}^{3D,M} & 0 & 0 & 0 \\ 0 & 0 & 0 & C_{44}^{3D,M} & 0 & 0 \\ 0 & 0 & 0 & 0 & C_{55}^{3D,M} & 0 \\ 0 & 0 & 0 & 0 & 0 & C_{66}^{3D,M} \end{bmatrix}}_{\hat{=}\mathbb{C}^{3D,M}} \underbrace{\begin{bmatrix} E_{11}^{3D,M} \\ E_{22}^{3D,M} \\ E_{33}^{3D,M} \\ 2E_{12}^{3D,M} \\ 2E_{23}^{3D,M} \\ 2E_{13}^{3D,M} \end{bmatrix}}_{\hat{=}\boldsymbol{E}^{3D,M}} = \underbrace{\begin{bmatrix} S_{11}^{3D,M} \\ S_{22}^{3D,M} \\ S_{33}^{3D,M} \\ S_{12}^{3D,M} \\ S_{23}^{3D,M} \\ S_{13}^{3D,M} \end{bmatrix}}_{\hat{=}\boldsymbol{S}_{\text{elast}}^{3D,M}}. \tag{36}$$

The parameters $C_{11}^{3D,M}$, $C_{22}^{3D,M}$ and $C_{44}^{3D,M}$ describe the in-plane stiffnesses of the solid-shell element analogous to the membrane stiffnesses of the 2D approach, cf. Eq. (13). The parameters $C_{33}^{3D,M}$, $C_{55}^{3D,M}$ and $C_{66}^{3D,M}$ describe the out-of-plane stiffnesses of the elements mid-plane ($\zeta^\star = 0$). In this context, $C_{33}^{3D,M}$ is the stiffness in the $\boldsymbol{e}_\zeta$-direction, respectively the compaction stiffness of the solid-shell element C_C, cf. Eq. (8). The parameters $C_{55}^{3D,M}$ and $C_{66}^{3D,M}$ are the shear stiffnesses in the ($\boldsymbol{e}_\zeta$-$\boldsymbol{e}_\xi$)- and ($\boldsymbol{e}_\zeta$-$\boldsymbol{e}_\eta$)-plane, corresponding to the transversal shear stiffnesses of the solid-shell element.

The elastic law for the bending behavior in Voigt-notation reads (cf. Eq. (2))

$$\underbrace{\begin{bmatrix} C_{11}^{3D,B} & 0 & 0 & 0 & 0 & 0 \\ 0 & C_{22}^{3D,B} & 0 & 0 & 0 & 0 \\ 0 & 0 & C_{33}^{3D,B} & 0 & 0 & 0 \\ 0 & 0 & 0 & C_{44}^{3D,B} & 0 & 0 \\ 0 & 0 & 0 & 0 & C_{55}^{3D,B} & 0 \\ 0 & 0 & 0 & 0 & 0 & C_{66}^{3D,B} \end{bmatrix}}_{\hat{=}\mathbb{C}^{3D,B}} \underbrace{\begin{bmatrix} E_{11}^{3D,B} \\ E_{22}^{3D,B} \\ E_{33}^{3D,B} \\ 2E_{12}^{3D,B} \\ 2E_{23}^{3D,B} \\ 2E_{13}^{3D,B} \end{bmatrix}}_{\hat{=}\boldsymbol{E}^{3D,B}} = \underbrace{\begin{bmatrix} S_{11}^{3D,B} \\ S_{22}^{3D,B} \\ S_{33}^{3D,B} \\ S_{12}^{3D,B} \\ S_{23}^{3D,B} \\ S_{13}^{3D,B} \end{bmatrix}}_{\hat{=}\boldsymbol{S}_{\text{elast}}^{3D,B}}. \tag{37}$$

The parameters $C_{11}^{3D,B}$, $C_{22}^{3D,B}$ and $C_{44}^{3D,B}$ describe the elastic bending behavior in the ($\boldsymbol{e}_\xi$-$\boldsymbol{e}_\eta$)-plane, analogous to the bending stiffnesses of the 2D approach, cf. Eq. (15). The parameter $C_{33}^{3D,B}$ describes the correlation between the compaction strains, which vary over the thickness of the solid-shell element, $E_{33}^{3D,B}$, and the corresponding bending stresses $S_{33}^{3D,B}$. Since varying compaction strains E_{33}^{B} lack physical meaning, the parameter $C_{33}^{3D,B}$ is set close to zero to inhibit the introduction of stresses or forces due to this deformation mode and prevent numerical instabilities. The parameters $C_{55}^{3D,B}$ and $C_{66}^{3D,B}$ describe the stiffnesses corresponding to varying transversal shear strains $E_{55}^{3D,B}$ and $E_{66}^{3D,B}$.

Poisson's ratios are not explicitly included in the elastic stiffness tensors $\mathbb{C}^{3D,M}$ and $\mathbb{C}^{3D,B}$, consistent with the earlier 2D approaches [16]. Their effects are implicitly captured through the isotropic assumption of the viscous material model. The viscous behavior for both the membrane and bending behavior follows an isotropic Newtonian model (Eq. (3)) extended by a nonlinear Cross viscosity law (Eq. (4)) analogous to the 2D approach, cf. (Section 3.1.2).

3.2.5. Remarks on the avoidance of locking phenomena for forming simulation of CoFRTPs

While the fundamental element formulation of the solid-shell element addresses the avoidance of transverse shear locking and volumetric locking phenomena, it does not inherently prevent tensile locking phenomena, which can occur in the case of highly anisotropic materials, such as CoFRTPs. In order to avoid tensile locking phenomena, the in-plane element edges are initially aligned in fiber direction $\boldsymbol{e}_1$ and transverse direction $\boldsymbol{e}_2$ of the blank, as recommended by ten Thije and Akkerman [79]. As we found this technique to be sufficient to prevent tensile locking, no further modifications to the element formulation were carried out. Note, that Hamila and Boisse [80,81] presented alternative approaches to circumventing tensile locking, involving modifications to the hourglass stabilization method. These approaches enable the utilization of unaligned meshes while preventing tensile locking phenomena.

The introduction of isotropic viscous contributions to the materials response induces Poisson effects even if the elastic part of the material model is free of Poisson effects. This can lead to volumetric locking phenomena, which are typically associated with nearly incompressible materials [40,72]. While the introduction of the EAS-DOF α_e in Eq. (21) effectively avoids volumetric locking in the thickness direction, no inherent prevention of volumetric locking phenomena in the in-plane directions is provided. However, the influence of volumetric locking phenomena in the in-plane directions is expected to be negligible due to the elevated material stiffness in fiber direction where the elastic forces are considerably higher than the viscous forces, effectively preventing Poisson effects in the ($\boldsymbol{e}_\xi$-$\boldsymbol{e}_\eta$)-plane and therefore preventing volumetric locking phenomena.

4. Transfer of material properties using coupon tests

4.1. Numerical setups for the coupon tests

In order to benefit from the reduced computational demands of the 2D approach for parameterization, an investigation is conducted into the transfer of in-plane and bending material properties from the element formulation employing the 2D approach outlined in Section 3.1 to the solid-shell element in Section 3.2. The workflow of transferring material parameters from the 2D approach to the 3D solid-shell approach is schematically summarized in Fig. 2. To prove the validity of the proposed workflow, a series of coupon tests are conducted using the finite element software Abaqus/Explicit. Three different loading conditions are considered: pure tension, simple shear and cantilever bending. The pure tension test and the simple shear test are employed to identify the in-plane material properties, whereas the cantilever bending test is utilized to assess the bending properties. The out-of-plane compaction behavior is parameterized based on the results of the compaction tests from Xiong et al. [53], cf. Section 2.2.

4.2. Transformation rule for the material properties from 2D to 3D

The material properties describing the membrane behavior of the solid-shell element (Section 3.2.4) are connected to the material properties of the 2D approach (Section 3.1.2) using the following calculation rules

$$\begin{aligned} &C_{11}^{3D,M} = E_F^{2D,M} + E_M^{2D,M}, && C_{22}^{3D,M} = E_M^{2D,M}, && C_{33}^{3D,M} = C_C\left(E_{33}^{M}\right), \\ &C_{44}^{3D,M} = \frac{1}{2}E_M^{2D,M}, && C_{55}^{3D,M} = C_{66}^{3D,M} = 10\ \text{MPa}, && \eta_0^{3D,M} = \eta_0^{2D,M}, \\ &\eta_\infty^{3D,M} = \eta_\infty^{2D,M}, && m^{3D,M} = m^{2D,M}, && n^{3D,M} = n^{2D,M}. \end{aligned} \tag{38}$$

The transverse shear stiffnesses $C_{55}^{3D,M}$ and $C_{66}^{3D,M}$ are set to 10 MPa, as these parameters have negligible influence on the simulation outcome, but contribute to overall numerical stability [63]. The compaction stiffness $C_C\left(E_{33}^{M}\right)$ is calculated at simulation runtime using the compaction model from Section 2.2.

The bending behavior of the solid-shell element is described using the same material parameters as for the 2D approach

$$\begin{aligned} &C_{11}^{3D,B} = C_{11}^{2D,B}, && C_{22}^{3D,B} = C_{22}^{2D,B}, && C_{33}^{3D,B} = 0.01\ \text{MPa}, \\ &C_{44}^{3D,B} = C_{12}^{2D,B}, && C_{55}^{3D,B} = C_{66}^{3D,B} = 10\ \text{MPa}, && \eta_0^{3D,B} = \eta_0^{2D,B}, \\ &\eta_\infty^{3D,B} = \eta_\infty^{2D,B}, && m^{3D,B} = m^{2D,B}, && n^{3D,B} = n^{2D,B}. \end{aligned} \tag{39}$$

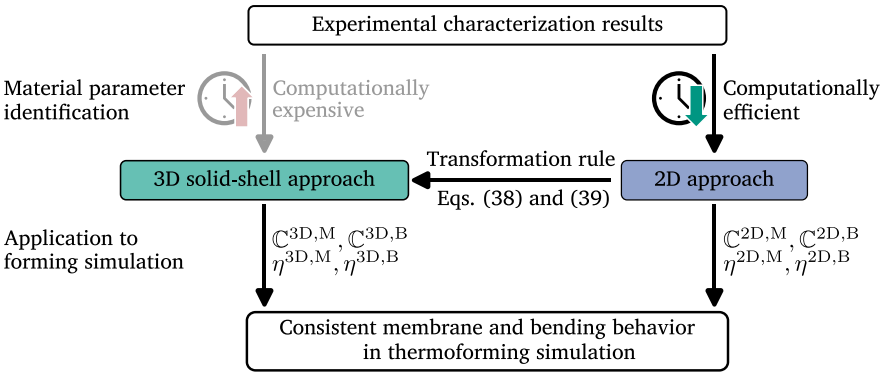

Fig. 2. Schematic of material parameter transfer from the 2D approach to the 3D solid-shell approach.

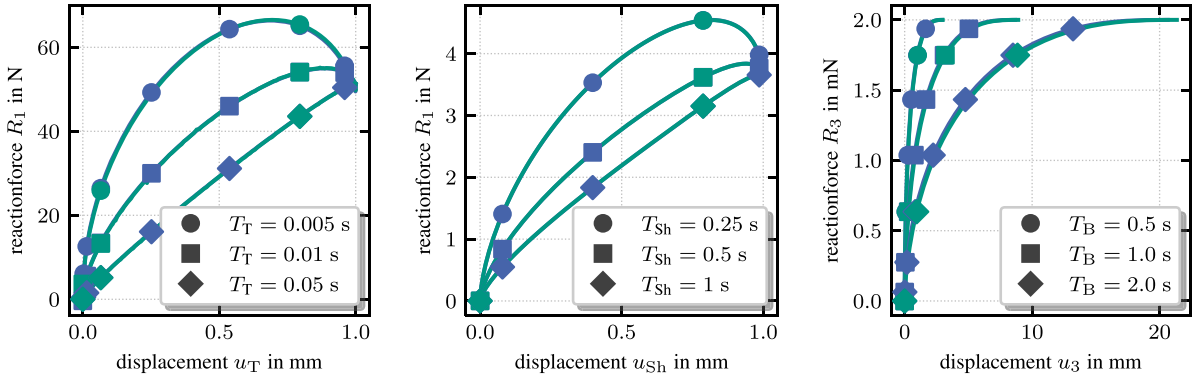

(a) Results for varying deformation rates $\dot{u}_M$ (b) Results for varying deformation rates $\dot{u}_{Sh}$ (c) Results for varying load rates $\dot{R}_3$

Fig. 3. Results for the numerical coupon tests (tensile, shear, bending) under varying load rates $\dot{u}_M$, $\dot{u}_{Sh}$ and $\dot{R}_3$ using the material parameter sets from Appendix B.

As the shear stiffnesses $C_{55}^{3D,B}$, and $C_{66}^{3D,B}$ have been demonstrated to exert minimal influence on the forming simulation results [63], they are each assigned a constant value of 10 MPa.

4.3. Numerical verification of transferability of material parameters from 2D to 3D

In order to verify that the proposed transformation rules (Eqs. (38) and (39)) for the material parameters from the 2D approach to the 3D solid-shell approach are valid, a series of numerical coupon tests are conducted. The numerical coupon tests are performed using the 2D approach from Section 3.1 and the 3D solid-shell element formulation from Section 3.2 with generic material parameters. The generic material parameters are summarized in Tables B.1–B.4 and satisfy the conditions in Eqs. (38) and (39).

The specimen for the tensile tests are $l_T = 60$ mm in length, $b_T = 10$ mm in width, and have a thickness of $t_T = 0.3$ mm. The specimen are fixed at the origin of the coordinate system, and the tension is applied displacement-controlled. The maximum displacement is attained at $u_T = 10$ mm. Different deformation rates $\dot{u}_T$ are achieved by applying the same maximum tip displacement u_T over different periods of time T_T. The results are compared using the reaction forces R_1 at the tip of the tensile rods.

The specimen for the simple shear test is $l_{Sh} = 5$ mm in length, $b_{Sh} = 5$ mm in width, and has a thickness of $t_{Sh} = 0.3$ mm. The specimen is fixed at the bottom, and the shearing is applied displacement-controlled. The maximum displacement is attained at $u_{Sh} = 1$ mm. Different deformation rates $\dot{u}_{Sh}$ are achieved by applying the same maximum tip displacement u_{Sh} over different periods of time T_{Sh}. The results are compared using the reaction forces R_1 at the top of the specimen.

The specimen for the cantilever bending test is $l_B = 60$ mm in length, $b_B = 10$ mm in width, and has a thickness of $t_B = 0.3$ mm. The beam is fixed at the origin of the coordinate system, and the bending boundary condition is applied at the tip of the beam force-controlled. The maximum force is attained at $R_3 = 2$ mN. The different load rates $\dot{R}_3$ are achieved by applying the same maximum load R_3 over different periods of time T_B. The results are compared using the curves of the applied reaction forces R_3 at the tip of the beam against the measured bending displacements u_3 at the tip of the beam.

The results of the numerical coupon tests for tensile, shear, and bending loading conditions are presented in Figs. 3(a), 3(b), and 3(c), respectively. For all three loading scenarios, the responses of the 3D solid-shell element (green) show good agreement with those of the 2D approach (blue) in the rate-dependent simulations. This verifies the successful transfer of material parameters from the 2D model to the 3D solid-shell element using the transformation rules given in Eqs. (38) and (39). As a result, the material characterization process for 3D solid-shell elements is significantly simplified, as it facilitates the utilization of computationally efficient 2D formulations for parameter identification of the 3D approach. Note that the 2D approach utilizes infinitesimal strain theory for the bending behavior (cf. Eq. (15)). Consequently, for large finite bending strains $\boldsymbol{E}^{3D,B}$, the results of the bending tests may deviate from the results of the solid-shell element formulation, which employs finite strain theory.

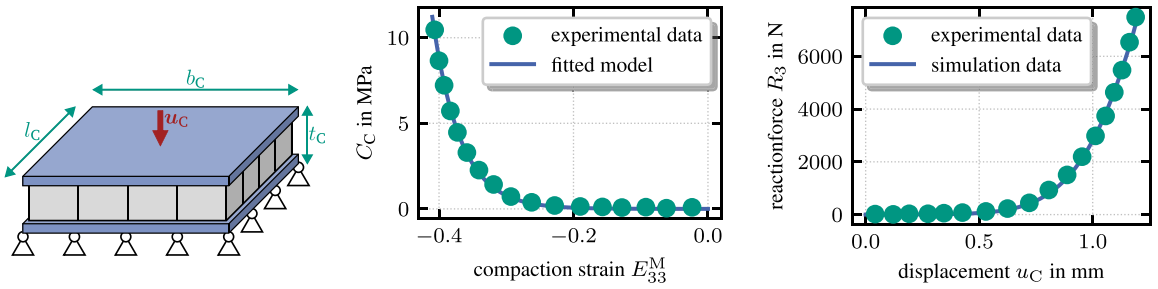

(a) Numerical setup for the compaction test

(b) Fitted compaction stiffness C_C

(c) Comparison of the compaction force with the experimental data [53]

Fig. 4. Numerical compaction test and comparison to the experimental data [53].

4.4. Parameterization of the compaction behavior

In order to parameterize the compaction behavior of the solid-shell element, compaction data from literature [53] is utilized. The test setup for the compaction test is illustrated in Fig. 4(a). The specimen for the compaction test is $l_C = 60$ mm in length, $b_C = 60$ mm in width, and has an initial thickness of $t_C = 2.05$ mm and is situated between two rigid plates. The plate on the bottom is fixed, while the plate on the top is displaced in normal direction with $u_C = 1.2$ mm. As the experimental trial was performed with a low compaction speed of 0.2 mm/s, the process can be considered quasi-static, and only the elastic compaction behavior is taken into account in the numerical compaction test. The numerical compaction test is performed using a single layer of solid-shell elements. The experimental data were digitalized using WebPlotDigitizer [82] and are displayed as green dots in Fig. 4(c).

For the nonlinear compaction behavior C_C, the compaction model (Eq. (8)) from Section 2.2 is employed. The parameters are identified numerically using a standard nonlinear least-squares fitting procedure implemented in Python. The resulting fitted parameters for C_C are

$$a = 5.58 \cdot 10^{-4} \text{ MPa}, \quad \text{and} \quad c = 2.416 \cdot 10^{1}. \tag{40}$$

For comparison, the corresponding compaction stiffness C_C^{exp} from experimental data is calculated using

$$C_C^{\text{exp}} = \frac{S_{33}^{\text{2PK}}}{E_{33}}. \tag{41}$$

and is presented in Fig. 4(b) using green dots. The curve of the fitted compaction stiffness C_C (blue) is in good agreement with the analytical compaction stiffness C_C^{exp} (green dots).

To validate the obtained nonlinear compaction model, the compaction stiffness C_C is implemented in the solid-shell element and numerical compaction tests, analogous to the setup shown in Fig. 4(a), are performed. The resulting curve of the compaction force R_3 versus the compaction displacement u_C is shown in Fig. 4(c) as a blue line. The simulation results are in good agreement with the experimental data from Xiong et al. [53] (green dots), confirming that the proposed model accurately captures the nonlinear compaction behavior of CoFRTPs. Furthermore, the results confirm that the analytical fitting procedure is effective in determining the compaction stiffness C_C.

5. Application on forming simulation

In this chapter, the 3D solid-shell element formulation is employed to simulate the thermoforming process of a single layer of CoFRTP in the finite element software Abaqus/Explicit. The rate-dependent material model and the nonlinear compaction behavior are employed to represent the complex mechanical response of the material. A double-domed tool geometry is selected to investigate the forming behavior under complex deformation conditions. The results are compared against those obtained using an experimentally validated 2D approach [21] (cf. lower half of Fig. 2) . Finally, the thickness distribution of the formed part is evaluated to assess the solid-shell element's capability to predict local thickness changes during forming.

5.1. Numerical test setup for forming simulation

An illustration of the numerical test setup is shown in Fig. 5. The double-dome tool geometry (green and blue) is a commonly used geometry in forming literature [e.g., 4,83], as it includes a double curved section that requires complex deformation modes to be formed. The punch and the die geometry are modeled as rigid surfaces. The forming process is implemented in a displacement-controlled manner, applying a Dirichlet boundary condition ($u = 60$ mm) over a time period of $T = 1$ s on the punch geometry, resulting in a minimum cavity thickness of $t = 0.2$ mm at the end of the forming process.

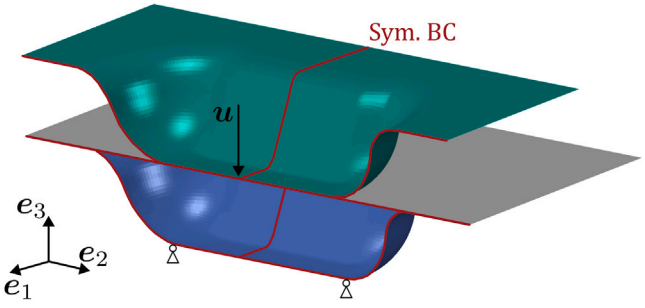

Fig. 5. Numerical test setup for the forming simulation of a double-domed geometry.

A single layer of CoFRTP (grey, cf. Fig. 5) is formed. The original blank dimensions are 502 mm × 310 mm × 0.3 mm which are discretized (in-plane) with the element edge length of $l_e = 5$ mm and a single element in thickness direction. The element edges are initially aligned in fiber direction e_1 and transverse direction e_2 of the blank to avoid tensile locking [79,80]. Given the twofold symmetry of the problem, only a quarter of the original problem is simulated (indicated by the red lines) resulting in a total of 1550 solid-shell elements. For the reference solution using the 2D approach, the blank is discretized with 6200 triangular shell elements. The contact between the blank and the forming tools is modeled using the general contact algorithm in Abaqus/Explicit. The tangential behavior is modeled using a Coulomb friction formulation with a friction coefficient of $\mu = 0.1$.

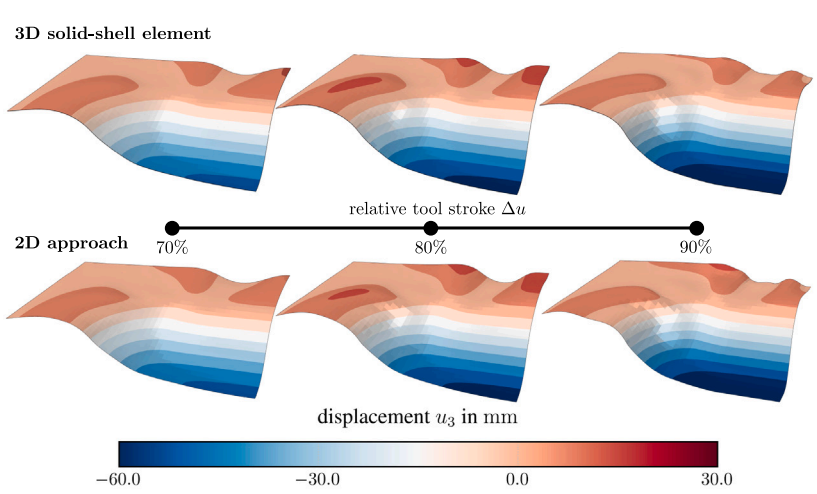

(a) Comparison of displacements u_3 at increasing tool strokes

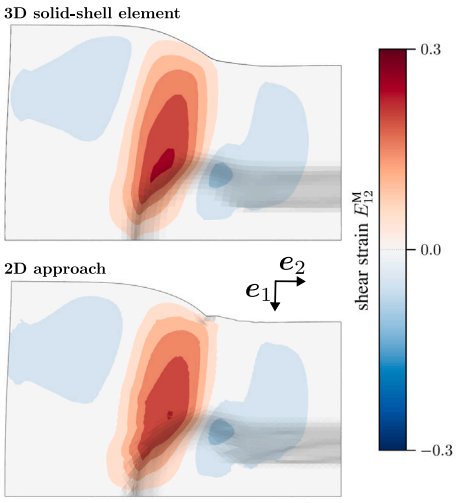

(b) Comparison of shear strain E_{12}^{M} at $\Delta u = 100\%$

Fig. 6. Comparison of the results using the 3D solid-shell versus the 2D approach using constant viscosity parameters.

Two material models are investigated. The first approach utilizes a simplified viscosity model, wherein viscosity parameters remain constant throughout the forming process (Newton model). This configuration serves as a reference to isolate the influence of time-dependent viscosity effects. In order to capture the rate-dependent behavior of the material in a more realistic manner, the second setup employs a nonlinear viscosity formulation based on the Cross model, as described in Eq. (4). The material parameters for both approaches are outlined in Tables C.5–C.8 and are based on in-house characterization trials for polypropylene reinforced with unidirectional glass fibers (PP-GF), following the methodology described by Dörr et al. [21]. Note, that the tensile stiffnesses in fiber direction are chosen well below the physically measured values for fiber stiffnesses but sufficiently high to numerically ensure the quasi-inextensibility condition of the fibers, which is a common assumption in forming simulation for composites [19,21]. A sensitivity analysis on forming speed for both the constant and cross-type viscosity models was conducted in Appendix D.

The simulations were executed on eight cores of an AMD EPYC 74F3 processor each. The simulations employing the cross viscosity model required approximately three minutes of computation time for the 2D-approach, while the 3D solid-shell simulations required approximately nine hours of computation time.

5.2. Results and discussion

5.2.1. Constant viscosity parameters

The forming simulation is conducted using constant viscosities ($\eta_\infty = \eta_0$) for the membrane and bending behavior to isolate the influence of time-dependent viscosity effects. The results of the forming simulation for both the 3D solid-shell and the 2D approach with constant viscosity parameters are shown in Fig. 6. A comparison of the global deformation behavior is conducted by evaluating the displacements u_3 at three representative stages of the forming process, corresponding to relative tool strokes $\Delta u = 70\%$, 80%, and 90% (Fig. 6(a)). The results demonstrate that wrinkle formation occurs at equivalent locations in both approaches and the maximum displacements u_3 are of comparable magnitude. The material draw-in and membrane shear strain at the end of the forming process ($\Delta u = 100\%$) are shown in Fig. 6(b) yielding significantly greater material draw-in in the fiber direction e_1 than in the transverse direction e_2 in a similar manner for both modeling approaches. Elevated shear strains E_{12}^{M} are observed in the double-curved regions of the blank, where substantial in-plane shear deformation is required to form the geometry yielding similar locations and magnitudes for both approaches. It can be concluded that the solid-shell element formulation is capable of capturing the global forming behavior in a manner analogous to the 2D approach.

5.2.2. Cross viscosity model

The results of the forming simulation using the Cross viscosity model (Eq. (4)) are presented in Fig. 7. A comparison of the global deformation behavior is conducted by evaluating the displacements u_3 at three representative stages of the forming process, corresponding to relative tool strokes $\Delta u = 70\%$, 80%, and 90% (Fig. 7(a)). The results demonstrate that wrinkle formation occurs at equivalent locations in both approaches and the maximum displacements u_3 are of comparable magnitude. In comparison to the case of constant viscosities from Section 5.2.1, the maximum displacements u_3 in positive e_3-direction are considerably lower. This is because thermoplastic tapes undergo two primary deformation modes during forming: in-plane shear and out-of-plane bending. When shear deformation is restricted due to high shear stiffness or viscosity, bending deformations are more probable to occur, leading to the formation of wrinkles. As the Cross viscosity model is employed, shear and bending viscosities, η^M and η^B, vary with local deformation rates, $\dot{\gamma}^M$ and $\dot{\gamma}^B$, respectively. For the given parameter set and tool geometry, this results in a lower effective shear viscosity η^M relative to the bending viscosity η^B, promoting shear-dominated deformation. Consequently, less wrinkles with lower amplitudes are observed in Fig. 7(a) than in Fig. 6(a). The material draw-in and membrane shear strain at the end of the forming process ($\Delta u = 100\%$) are shown in Fig. 7(b) yielding significantly greater material draw-in in the fiber direction e_1 than in the transverse direction e_2 in a similar manner for both modeling approaches. Elevated shear strains E_{12}^{M} are observed in the double-curved regions of the blank, where substantial in-plane shear deformation is required to form the geometry yielding similar locations and magnitudes for both approaches. It can be concluded that the 3D solid-shell element formulation with the employed Cross viscosity model is capable of capturing the nonlinear viscosity behavior and the global forming behavior of the blank in a similar manner as the 2D approach.

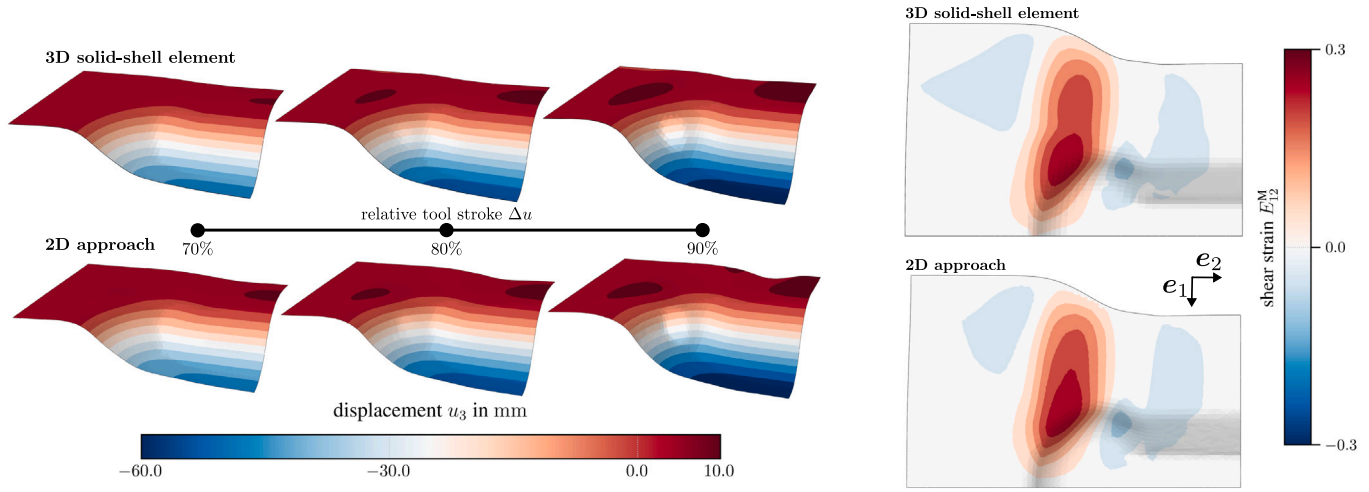

(a) Comparison of displacements u_3 at increasing tool strokes

(b) Comparison of shear strain E_{12}^{M} at $\Delta u = 100\%$

Fig. 7. Comparison of the results using the 3D solid-shell versus the 2D approach using the Cross viscosity model.

5.2.3. Compaction behavior

In contrast to the 2D approach, the 3D solid-shell element formulation enables the prediction of local thickness changes during the forming process. The final thickness distribution t at $\Delta u = 100\%$ is shown in Fig. 8. To aid visual interpretation, the right-hand side of the figure includes the double-dome tool geometry overlaid on the blank, illustrating the regions in contact during the compaction phase of forming. The thickness is calculated as the ratio of the solid-shell element's volume V_{e} to the average of its top and bottom surface areas A^{Top} and A^{Bot}

$$t = \frac{2V_{\mathrm{e}}}{A^{\mathrm{Top}} + A^{\mathrm{Bot}}}. \tag{42}$$

The elements volume V_{e} and surface areas A^{Top} and A^{Bot} can obtained from the element's node coordinates $\boldsymbol{x}_I$. The results of the elements' thicknesses indicates that the elements are compacted to a desired cavity thickness of $t = 0.2$ mm at all locations where the blank is in contact with the forming tools. In locations where the blank does not make contact with the tools, the thickness remains close to its initial value of $t_0 = 0.3$ mm. In regions where the blank bends around the tool radii, the thickness is reduced further, falling below $t = 0.2$ mm. This phenomenon can be attributed to the high curvature present in these regions, which generates increased transverse pressure as the blank is forced into the cavity.

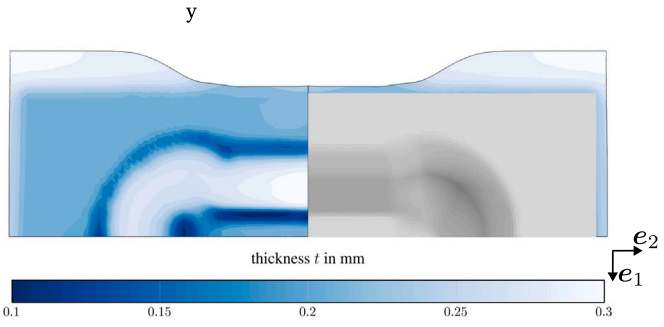

Fig. 8. Resulting thickness distribution t of the forming simulation of a double-domed geometry.

In summary, the results qualitatively align with the anticipated outcome of compaction behavior during thermoforming and are also consistent with those shown in Xiong et al. [52,53], Poppe et al. [56] and Schäfer [78], who also used a double-dome geometry to demonstrate through-thickness behavior. A direct quantitative comparison with experimental data is not feasible at this stage because thermoforming FRTPs with a single reinforcement direction under controlled conditions is challenging due to tearing in the unsupported transverse direction. The present results should therefore be seen as a first methodological demonstration of the solid-shell element's capability, with experimental validation identified as an essential step for future work.

6. Conclusion and outlook

In this work, a novel finite 3D element formulation based on an 8-node hexahedral solid-shell element was developed for the macroscopic simulation of the thermoforming process of CoFRTPs. This formulation enhances previous works by including rate-dependent material behavior. The solid-shell element is implemented as a VUEL user subroutine in the commercial finite element software ABAQUS/Explicit. The element incorporates several numerical techniques to prevent numerical locking phenomena, such as the EAS- and the ANS-concept and utilizes a tailored hourglass control scheme suitable for highly anisotropic and viscous materials, along with a membrane-bending decomposition technique.

As the characterization of the viscoelastic material model within the solid-shell element is numerically expensive, the transferability of material parameters from a 2D approach to the developed 3D solid-shell element was investigated through a series of numerical coupon tests. This facilitates the reuse of existing material datasets and significantly reduces computational expenses associated with material parameter identification. To access the performance of the developed 3D solid-shell element formulation, comparisons of the simulation results were conducted against those obtained from an experimentally validated 2D simulation approach. Good agreement was observed between the two methods in terms of global forming behavior, material draw-in, and shear distribution, indicating that the 3D solid-shell formulation is capable of accurately capturing the key deformation mechanisms involved in the thermoforming of CoFRTPs. The evaluation of the resulting final thickness distribution yielded qualitatively expected results, thereby demonstrating the solid-shell element's ability to predict local thickness changes during the forming process which is a significant advantage compared to the 2D approach.

In summary, the proposed 3D solid-shell element formulation represents a substantial advancement in the numerical simulation of thermoforming processes for CoFRTPs. This advancement provides a more comprehensive understanding and prediction of the final part geometry, the final thickness distribution and the local fiber volume content and establishes a foundation for downstream simulation steps, including warpage and demolding simulations. Future work will include direct experimental validation of the 3D solid-shell element formulation, focusing on both the global deformation behavior and the local thickness distribution. This will involve comparing simulation results with thermoforming test data ensuring that the employed material model accurately captures the rate-dependent behavior of CoFRTPs. If discrepancies are observed, this validation will guide enhancements to the constitutive model, such as the adoption of a multi-mode viscoelastic formulation for improving accuracy. Further enhancements of the 3D solid-shell element formulation will be pursued by integrating a temperature degree of freedom. This integration will enable thermoforming simulation under varying thermal conditions, including prediction of through-thickness thermal gradients, temperature-dependent material properties, and crystallization. Beyond material modeling, the developed solid-shell formulation will be optimized in terms of computational performance. Afterwards, it will be applied to more complex geometries and multi-layered CoFRTP structures to assess its robustness and effectiveness in practical, industrial-scale thermoforming scenarios.

CRediT authorship contribution statement

Johannes Mitsch: Writing – original draft, Visualization, Validation, Software, Methodology, Investigation, Formal analysis, Conceptualization. **Bastian Schäfer:** Writing – review & editing, Software, Methodology, Conceptualization. **Luise Kärger:** Writing – review & editing, Supervision, Funding acquisition, Conceptualization.

Acknowledgments

This work is part of the DFG AI Research Unit 5339 (project no. 459291153) funded by the Deutsche Forschungsgemeinschaft, Germany (DFG, German Research Foundation) to advance the development of a CAE chain for stamp forming processes. It is also part of the DFG-funded Heisenberg project “Digitalization of fiber-reinforced polymer processes for resource-efficient manufacturing of lightweight components” (project no. 455807141).

Declaration of competing interest

The authors declare that they have no known competing financial interests or personal relationships that could have appeared to influence the work reported in this paper.

Appendix A. Calculation of the hourglass stresses for viscoelastic material model

Using the Voigt-Kelvin model (cf. Eq. (1)), the viscoelastic stress is given by

$$\boldsymbol{S}^{\mathrm{2PK}} = \boldsymbol{S}^{\mathrm{2PK}}_{\mathrm{elas}} + \boldsymbol{S}^{\mathrm{2PK}}_{\mathrm{visc}}, \tag{A.1}$$

where the elastic part is solely dependent on the elastic strain $\boldsymbol{E}$ (cf. Eq. (2))

$$\boldsymbol{S}^{\mathrm{2PK}}_{\mathrm{elas}} = \mathbb{C}\,[\boldsymbol{E}] \tag{A.2}$$

and the viscous part is only dependent on the deformation rate tensor $\boldsymbol{D}$ (cf. Eq. (1))

$$\boldsymbol{\sigma}_{\mathrm{visc}} = \eta \boldsymbol{D}. \tag{A.3}$$

Using Eq. (6), the viscous part of the second Piola–Kirchhoff stress tensor $\boldsymbol{S}^{\mathrm{2PK}}_{\mathrm{visc}}$ is given by

$$\boldsymbol{S}^{\mathrm{2PK}}_{\mathrm{visc}} = J\eta\, \boldsymbol{F}^{-1}\boldsymbol{D}\boldsymbol{F}^{-\mathsf{T}} = J\eta\, \boldsymbol{F}^{-1}\boldsymbol{F}^{-\mathsf{T}}\dot{\boldsymbol{E}}\boldsymbol{F}^{-1}\boldsymbol{F}^{-\mathsf{T}} = J\eta\, \boldsymbol{C}^{-1}\dot{\boldsymbol{E}}\boldsymbol{C}^{-1}, \tag{A.4}$$

depending on the strain rate tensor $\dot{\boldsymbol{E}}$ and utilizing the right Cauchy–Green tensor $\boldsymbol{C} = \boldsymbol{F}^{\mathsf{T}}\boldsymbol{F}$.

To calculate the contribution of the viscous stresses to the hourglass forces, the derivative of the stress $\boldsymbol{S}^{\mathrm{2PK}}$ with respect to the strain rate $\dot{\boldsymbol{E}}$ is calculated. As the elastic part of the stress $\boldsymbol{S}^{\mathrm{2PK}}_{\mathrm{elast}}(\boldsymbol{E}) = \mathbb{C}\,[\boldsymbol{E}]$ is independent of the strain rate $\dot{\boldsymbol{E}}$ the derivative of the elastic stress with respect to the strain rate $\dot{\boldsymbol{E}}$ is zero. The derivative of the viscous part of the stress $\boldsymbol{S}^{\mathrm{2PK}}_{\mathrm{visc}}(\dot{\boldsymbol{E}})$ with respect to the strain rate $\dot{\boldsymbol{E}}$ is calculated

$$\begin{aligned}\frac{\partial S^{\mathrm{2PK}}_{\mathrm{visc},ij}}{\partial \dot{E}_{kl}} &= \frac{\partial}{\partial \dot{E}_{kl}}\left(J\eta\, C^{-1}_{im}\dot{E}_{mn}C^{-1}_{nj}\right)\\ &= \frac{J\eta}{2}\left(C^{-1}_{im}\left(\delta_{mk}\delta_{nl}+\delta_{lm}\delta_{nk}\right)C^{-1}_{nj}\right)\\ &= \frac{J\eta}{2}\left(C^{-1}_{ik}C^{-1}_{lj}+C^{-1}_{il}C^{-1}_{kj}\right) = V^{\star}_{ijkl},\end{aligned} \tag{A.5}$$

which reads in symbolic notation

$$\frac{\partial \boldsymbol{S}^{\mathrm{2PK}}_{\mathrm{visc}}(\dot{\boldsymbol{E}})}{\partial \dot{\boldsymbol{E}}} = \frac{J\eta}{2}\left(\boldsymbol{C}^{-1}\square\boldsymbol{C}^{-1} + \left(\boldsymbol{C}^{-1}\square\boldsymbol{C}^{-1}\right)^{\mathsf{T_R}}\right) = \mathbb{V}^{\star}. \tag{A.6}$$

Here, δ_{ij} denotes the Kronecker symbol. The product $\boldsymbol{A}\square\boldsymbol{B}$ is defined $(\boldsymbol{A}\square\boldsymbol{B})\,[\boldsymbol{C}] = \boldsymbol{A}\boldsymbol{C}\boldsymbol{B}$. The tensor $\mathbb{V}^{\star}$ is the hourglass viscosity tensor introduced in Eq. (34). Note, that if a symmetric second-order tensor $\boldsymbol{A} \in Sym$ is applied on the result of Eq. (A.5) simplifies to

$$\begin{aligned}\frac{\partial S^{\mathrm{2PK}}_{\mathrm{visc},ij}}{\partial \dot{E}_{kl}} A_{kl} &= \frac{1}{2}\frac{\partial S^{\mathrm{2PK}}_{\mathrm{visc},ij}}{\partial \dot{E}_{kl}}\left(A_{kl}+A^{\mathsf{T}}_{kl}\right)\\ &= \frac{J\eta}{4}\left(C^{-1}_{ik}C^{-1}_{lj}+C^{-1}_{il}C^{-1}_{kj}\right)\left(A_{kl}+A_{lk}\right)\\ &= \frac{J\eta}{4}\left(C^{-1}_{ik}C^{-1}_{lj}A_{kl}+C^{-1}_{il}C^{-1}_{kj}A_{kl}+C^{-1}_{il}C^{-1}_{kj}A_{kl}+C^{-1}_{ik}C^{-1}_{lj}A_{kl}\right)\\ &= J\eta C^{-1}_{ik}C^{-1}_{lj}A_{kl} \quad \forall \boldsymbol{A} \in Sym.\end{aligned} \tag{A.7}$$

The symbolic representation of Eq. (A.7) reads

$$\frac{\partial \boldsymbol{S}^{\mathrm{2PK}}_{\mathrm{visc}}(\dot{\boldsymbol{E}})}{\partial \dot{\boldsymbol{E}}}\,[\boldsymbol{A}] = \mathbb{V}^{\star}[\boldsymbol{A}] = J\eta\left(\boldsymbol{C}^{-1}\square\boldsymbol{C}^{-1}\right)\,[\boldsymbol{A}] = J\eta\,\boldsymbol{C}^{-1}\boldsymbol{A}\boldsymbol{C}^{-1} \quad \forall \boldsymbol{A} \in Sym. \tag{A.8}$$

Appendix B. Material parameters for the numerical coupon tests

Table B.1
Viscoelastic membrane material parameters for the 2D approach in the coupon tests.

$E^{\mathrm{2D,M}}_{\mathrm{F}}$ MPa	$E^{\mathrm{2D,M}}_{\mathrm{M}}$ MPa	$G^{\mathrm{2D,M}}_{\mathrm{M}}$ MPa	$\eta^{\mathrm{2D,M}}_{0}$ MPa s	$\eta^{\mathrm{2D,M}}_{\infty}$ MPa s	$m^{\mathrm{2D,M}}$ –	$n^{\mathrm{2D,M}}$ –
980.0	20.0	10.0	4.0	1.0	50.9773	0.4655

Table B.2
Viscoelastic bending material parameters for the 2D approach in the coupon tests.

$C^{\mathrm{2D,B}}_{11}$ MPa	$C^{\mathrm{2D,B}}_{22}$ MPa	$C^{\mathrm{2D,B}}_{12}$ MPa	$\eta^{\mathrm{2D,B}}_{0}$ MPa s	$\eta^{\mathrm{2D,B}}_{\infty}$ MPa s	$m^{\mathrm{2D,B}}$ –	$n^{\mathrm{2D,B}}$ –
100.0	100.0	1.0	500.0	10.0	41.7412	0.6877

Table B.3
Viscoelastic membrane material parameters for the 3D approach in the coupon tests.

$C^{\mathrm{3D,M}}_{11}$ MPa	$C^{\mathrm{3D,M}}_{22}$ MPa	$C^{\mathrm{3D,M}}_{33}$ MPa	$C^{\mathrm{3D,M}}_{44}$ MPa	$C^{\mathrm{3D,M}}_{55}$ MPa	$C^{\mathrm{3D,M}}_{66}$ MPa	$\eta^{\mathrm{3D,M}}_{0}$ MPa s	$\eta^{\mathrm{3D,M}}_{\infty}$ MPa s	$m^{\mathrm{3D,M}}$ –	$n^{\mathrm{3D,M}}$ –
100.0	20.0	20.0	10.0	10.0	10.0	4.0	1.0	50.9773	0.4655

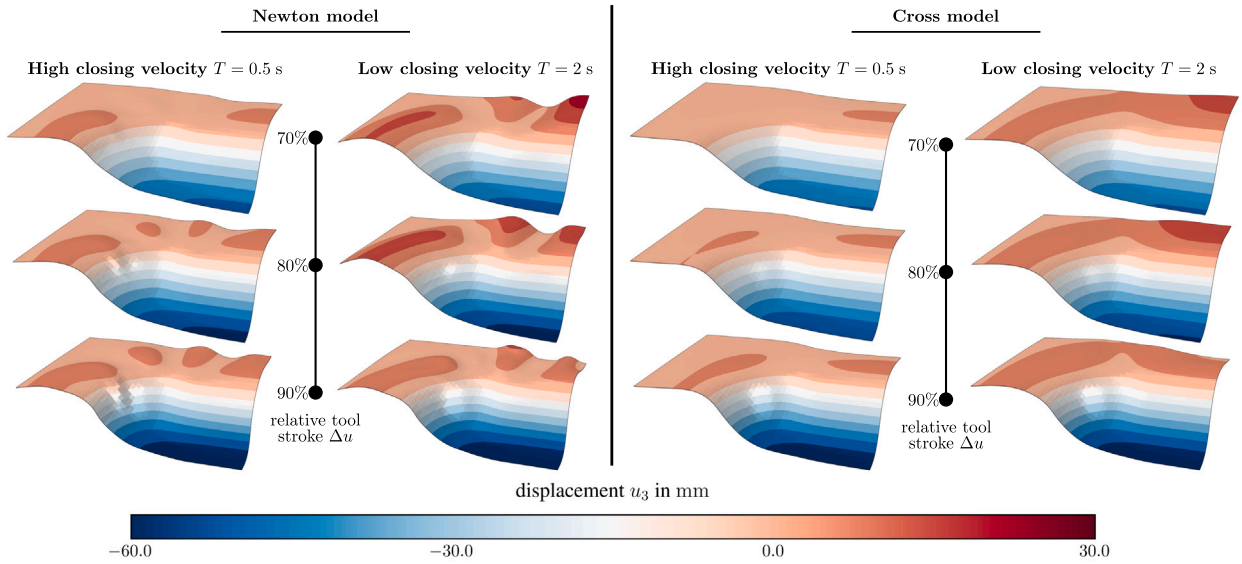

Fig. C.9. Analysis of the rate-dependent material model with respect to the forming velocity.

Table B.4
Viscoelastic bending material parameters for the 3D approach in the coupon tests.

$C_{11}^{3D,B}$ MPa	$C_{22}^{3D,B}$ MPa	$C_{33}^{3D,B}$ MPa	$C_{44}^{3D,B}$ MPa	$C_{55}^{3D,B}$ MPa	$C_{66}^{3D,B}$ MPa	$\eta_0^{3D,B}$ MPa s	$\eta_\infty^{3D,B}$ MPa s	$m^{3D,B}$ –	$n^{3D,B}$ –
100.0	100.0	0.01	1.0	10.0	10.0	500.0	10.0	41.7412	0.6877

Appendix C. Material parameters for the forming simulation

C.1. Material parameters for the 2D approach using superimposed conventional shell elements

Table C.5
Viscoelastic model parameters for PP-GF of the membrane behavior of the conventional shell elements.

Model	$E_F^{2D,M}$ MPa	$E_M^{2D,M}$ MPa	$G_M^{2D,M}$ MPa	$\eta_0^{2D,M}$ MPa s	$\eta_\infty^{2D,M}$ MPa s	$m^{2D,M}$ –	$n^{2D,M}$ –
Newton	1000.0	0.0147	0.00735	0.1	0.1	–	–
Cross	1000.0	0.0147	0.00735	0.4	0.0	50.9773	0.4655

Table C.6
Viscoelastic model parameters for PP-GF of the bending behavior of the conventional shell elements.

Model	$C_{11}^{2D,B}$ MPa	$C_{22}^{2D,B}$ MPa	$C_{12}^{2D,B}$ MPa	$\eta_0^{2D,B}$ MPa s	$\eta_\infty^{2D,B}$ MPa s	$m^{2D,B}$ –	$n^{2D,B}$ –
Newton	75.8971	0.7589	0.37948	10.0	10.0	–	–
Cross	75.8971	0.7589	0.37948	500.0	0.0	41.7412	0.6877

C.2. Material parameters for the 3D approach using hexahedral solid-shell elements

Table C.7
Viscoelastic model parameters for PP-GF of the membrane behavior of the solid-shell elements.

Model	$C_{11}^{3D,M}$ MPa	$C_{22}^{3D,M}$ MPa	$C_{33}^{3D,M}$ MPa	$C_{44}^{3D,M}$ MPa	$C_{55}^{3D,M}$ MPa	$C_{66}^{3D,M}$ MPa	$\eta_0^{3D,M}$ MPa s	$\eta_\infty^{3D,M}$ MPa s	$m^{3D,M}$ –	$n^{3D,M}$ –
Newton	1000.0147	0.0147	C_C	0.00735	10.0	10.0	0.1	0.1	–	–
Cross	1000.0147	0.0147	C_C	0.00735	10.0	10.0	0.4	0.0	50.9773	0.4655

Table C.8
Viscoelastic model parameters for PP-GF of the bending behavior of the solid-shell elements.

Model	$C_{11}^{3D,B}$ MPa	$C_{22}^{3D,B}$ MPa	$C_{33}^{3D,B}$ MPa	$C_{44}^{3D,B}$ MPa	$C_{55}^{3D,B}$ MPa	$C_{66}^{3D,B}$ MPa	$\eta_0^{3D,B}$ MPa s	$\eta_\infty^{3D,B}$ MPa s	$m^{3D,B}$ –	$n^{3D,B}$ –
Newton	75.8971	0.758971	0.01	0.37948	10.0	10.0	10.0	10.0	–	–
Cross	75.8971	0.758971	0.01	0.37948	10.0	10.0	500.0	0.0	41.7412	0.6877

Appendix D. Sensitivity analysis of the rate-dependent material model

To assess the sensitivity of the global deformation behavior to variations in forming velocity, simulations were performed using the 3D solid-shell element. As material parameters, the viscoelastic material behavior with constant viscosity parameters (Newton model) and Cross viscosity parameters (Cross model) were used, cf. Tables C.7 and C.8. The simulation setup is the same as that described in Section 5.1. Two forming velocities were considered, corresponding to press-closing times of $T = 0.5$ s and $T = 2.0$ s, respectively.

The results indicate that the Newton model (left-hand side of Fig. C.9) produces significantly more wrinkles with higher amplitudes than the Cross model (right-hand side of Fig. C.9), which is consistent with the findings in Section 5.2. For both models, the wrinkling amplitudes are higher at the lower forming velocity ($T = 2.0$ s) compared to the higher forming velocity ($T = 0.5$ s). This behavior may be attributed to higher bending viscosities relative to membrane viscosities. This effect is further superimposed by the non-linear (shear-thinning) viscosity models in case of the Cross model. Since the membrane-to-bending viscosity ratio depends on the specific viscosity parameters, these trends may vary for other material properties or geometries.

In summary, the global deformation behavior is strongly affected by forming velocity, highlighting the impact of incorporating rate-dependent material behavior in forming simulations.

Data availability

Data will be made available on request.

References

[1] Vanclooster K, van Goidsenhoven S, Lomov SV, Verpoest I. Optimizing the deepdrawing of multilayered woven fabric composites. Int J Mater Form 2009;2(1):153.

[2] Lessard H, Lebrun G, Benkaddour A, Pham X-T. Influence of process parameters on the thermostamping of a [0/90]12 carbon/polyether ether ketone laminate. Compos Part A: Appl Sci Manuf 2015;70:59–68.

[3] Breuer U, Neitzel M, Ketzer V, Reinicke R. Deep drawing of fabric-reinforced thermoplastics: Wrinkle formation and their reduction. Polym Compos 1996;17(4):643–7.

[4] Harrison P, Gomes R, Curado-Correia N. Press forming a 0/90 cross-ply advanced thermoplastic composite using the double-dome benchmark geometry. Compos Part A: Appl Sci Manuf 2013;54:56–69.

[5] Zeeb G, Mitsch J, Wilhelm M, Kärger L, Henning F. Influence of gripper positions on the formation of wrinkles during the thermoforming process of thermoplastic UD-tape laminates. In: Materials research proceedings, vol. 54, Materials Research Forum LLC; 2025, p. 544–53.

[6] Joppich T, Dörr D, van der Meulen L, Link T, Hangs B, Henning F. Layup and process dependent wrinkling behavior of PPS/CF UD tape-laminates during non-isothermal press forming into a complex component. In: AIP conference proceedings 1769, 170011. 2016, 170012.

[7] Brands D, di Genova LG, Pierik ER, Grouve WJB, Wijskamp S, Akkerman R. Formability experiments for unidirectional thermoplastic composites. Key Eng Mater 2022;926:1358–71.

[8] Kärger L, Galkin S, Zimmerling C, Dörr D, Linden J, Oeckerath A, Wolf K. Forming optimisation embedded in a CAE chain to assess and enhance the structural performance of composite components. Compos Struct 2018;192:143–52.

[9] Chen H, Li S, Wang J, Ding A. A focused review on the thermo-stamping process and simulation progresses of continuous fibre reinforced thermoplastic composites. Compos Part B: Eng 2021;224:109196.

[10] Boisse P, Colmars J, Hamila N, Naouar N, Steer Q. Bending and wrinkling of composite fiber preforms and prepregs. A review and new developments in the draping simulations. Compos Part B: Eng 2018;141:234–49.

[11] Boisse P, Akkerman R, Carlone P, Kärger L, Lomov SV, Sherwood JA. Advances in composite forming through 25 years of ESAFORM. Int J Mater Form 2022;15(3):99.

[12] Gunjal H, Singh G. Chapter 8 Review of optimization and simulation approaches for thermoplastic composite design. In: Green composites manufacturing. De Gruyter; 2024, p. 173–98.

[13] Guzman Maldonado E, Bigot N, Denis Y, Hamila N. 13 - Thermomechanical modeling and experimental characterization of continuous fiber-reinforced thermoplastic composites at forming temperatures. In: Wang P, Hamila N, editors. Advanced structural textile composites forming. Woodhead publishing series in composites science and engineering, Woodhead Publishing; 2025, p. 355–88.

[14] Parlevliet PP, Bersee HEN, Beukers A. Residual stresses in thermoplastic composites – a study of the literature. Part III: Effects of thermal residual stresses. Compos Part A: Appl Sci Manuf 2007;38(6):1581–96.

[15] Lu X, Ding J, Peng X, Sun G, Wang X, Yue W, Zhou H, Huang Z, Zhou H, Mai YW. A focused review of the draping process and its impact on the resin infusion in liquid composite molding. Thin-Walled Struct 2024;205:112362.

[16] Dörr D. Simulation of the thermoforming process of UD fiber-reinforced thermoplastic tape laminates (Dissertation), Karlsruhe; 2019.

[17] Soulat D, Cheruet A, Boisse P. Simulation of continuous fibre reinforced thermoplastic forming using a shell finite element with transverse stress. Comput Struct 2006;84(13–14):888–903.

[18] Boisse P, Hamila N, Vidal-Sallé E, Dumont F. Simulation of wrinkling during textile composite reinforcement forming. Influence of tensile, in-plane shear and bending stiffnesses. Compos Sci Technol 2011;71(5):683–92.

[19] Allaoui S, Boisse P, Chatel S, Hamila N, Hivet G, Soulat D, Vidal-Salle E. Experimental and numerical analyses of textile reinforcement forming of a tetrahedral shape. Compos Part A: Appl Sci Manuf 2011;42(6):612–22.

[20] Haanappel SP, Thije R, Sachs U, Rietman B, Akkerman R. Formability analyses of uni-directional and textile reinforced thermoplastics. Compos Part A: Appl Sci Manuf 2014;56:80–92.

[21] Dörr D, Schirmaier FJ, Henning F, Kärger L. A viscoelastic approach for modeling bending behavior in finite element forming simulation of continuously fiber reinforced composites. Compos Part A: Appl Sci Manuf 2017;94:113–23.

[22] Dörr D, Joppich T, Kugele D, Henning F, Kärger L. A coupled thermomechanical approach for finite element forming simulation of continuously fiber-reinforced semi-crystalline thermoplastics. Compos Part A: Appl Sci Manuf 2019;125.

[23] Poppe C, Rosenkranz T, Dörr D, Kärger L. Comparative experimental and numerical analysis of bending behaviour of dry and low viscous infiltrated woven fabrics. Compos Part A: Appl Sci Manuf 2019;124:105466.

[24] Thije R, Akkerman R, Huétink J. Large deformation simulation of anisotropic material using an updated Lagrangian finite element method. Comput Methods Appl Mech Engrg 2007;196(33–34):3141–50.

[25] Skordos AA, Monroy Aceves C, Sutcliffe M. A simplified rate dependent model of forming and wrinkling of pre-impregnated woven composites. Compos Part A: Appl Sci Manuf 2007;38(5):1318–30.

[26] Guzman-Maldonado E, Hamila N, Naouar N, Moulin G, Boisse P. Simulation of thermoplastic prepreg thermoforming based on a visco-hyperelastic model and a thermal homogenization. Mater Des 2016;93:431–42.

[27] Dörr D, Henning F, Kärger L. Nonlinear hyperviscoelastic modelling of intra-ply deformation behaviour in finite element forming simulation of continuously fibre-reinforced thermoplastics. Compos Part A: Appl Sci Manuf 2018.

[28] Alshahrani H, Hojjati M. Bending behavior of multilayered textile composite prepregs: Experiment and finite element modeling. Mater Des 2017;124:211–24.

[29] Donderwinkel TG, Rietman B, Haanappel SP, Akkerman R. Stamp forming optimization for formability and crystallinity. In: AIP conference proceedings 1769, 170011. 2016, 170029.

[30] Street GE, Johnson MS. The intra-ply shear behaviour of non-isothermal thermoplastic composite laminates. J Compos Sci 2023;7(10):432.

[31] Dörr D, Kugele D, Joppich T, Henning F, Kärger L. On the relevance of thermomechanics and crystallization kinetics for FE thermoforming simulation of semi-crystalline thermoplastic tapes. In: Proceedings of the 22nd international ESAFORM conference on material forming: ESAFORM 2019. Vitoria-Gasteiz, Spain; 2019, 020011.

[32] Bigot N, Guzman-Maldonado E, Boutaous M, Xin S, Hamila N. A coupled thermo-mechanical modelling strategy based on alternating direction implicit formulation for the simulation of multilayered CFRTP thermo-stamping process. Appl Compos Mater 2022;29(6):2321–41.

[33] Lévy A, Hoang DA, Le Corre S. On the alternate direction implicit (ADI) method for solving heat transfer in composite stamping. Mater Sci Appl 2017;08(01):37–63.

[34] Bigot N, Hamila N, Chaudet P, Xin S, Boutaous M. Modeling and experimental identification of thermo-kinetic and visco-hyperelastic coupling for semicrystalline thermoplastic continuous fiber composites subjected to processing temperatures. Compos Part A: Appl Sci Manuf 2024;178:107967.

[35] Cardoso RPR, Yoon JW, Mahardika M, Choudhry S, Alves de Sousa RJ, Fontes Valente RA. Enhanced assumed strain (EAS) and assumed natural strain (ANS) methods for one-point quadrature solid-shell elements. Internat J Numer Methods Engrg 2008;75(2):156–87.

[36] Pagani M, Reese S, Perego U. Computationally efficient explicit nonlinear analyses using reduced integration-based solid-shell finite elements. Comput Methods Appl Mech Engrg 2014;268:141–59.

[37] Schwarze M, Vladimirov IN, Reese S. Sheet metal forming and springback simulation by means of a new reduced integration solid-shell finite element technology. Comput Methods Appl Mech Engrg 2011;200(5–8):454–76.

[38] Rah K, van Paepegem W, Habraken AM, Sousa RA, Valente RAF. Evaluation of different advanced finite element concepts for detailed stress analysis of laminated composite structures. Int J Mater Form 2009;2(S1):943–7.

[39] Schwarze M, Reese S. A reduced integration solid-shell finite element based on the EAS and the ANS concept-geometrically linear problems. Internat J Numer Methods Engrg 2009;80(10):1322–55.

[40] Schwarze M, Reese S. A reduced integration solid-shell finite element based on the EAS and the ANS concept-large deformation problems. Internat J Numer Methods Engrg 2011;85(3):289–329.

[41] Mostafa M. An improved solid-shell element based on ANS and EAS concepts. Internat J Numer Methods Engrg 2016;108(11):1362–80.

[42] Hauptmann R, Schweizerhof K. A systematic development of 'solid-shell' element formulations for linear and non-linear analyses employing only displacement degrees of freedom. Internat J Numer Methods Engrg 1998;42(1):49–69.

[43] Hauptmann R, Schweizerhof K, Doll S. Extension of the 'solid-shell' concept for application to large elastic and large elastoplastic deformations. Internat J Numer Methods Engrg 2000;49(9):1121–41.

[44] Hauptmann R, Doll S, Harnau M, Schweizerhof K. 'Solid-shell' elements with linear and quadratic shape functions at large deformations with nearly incompressible materials. Comput Struct 2001;79(18):1671–85.

[45] Mattern S, Schmied C, Schweizerhof K. Highly efficient solid and solid-shell finite elements with mixed strain–displacement assumptions specifically set up for explicit dynamic simulations using symbolic programming. Comput Struct 2015;154:210–25.

[46] Reese S, Wriggers P, Reddy BD. A new locking-free brick element technique for large deformation problems in elasticity. Comput Struct 2000;75(3):291–304.

[47] Reese S. A large deformation solid-shell concept based on reduced integration with hourglass stabilization. Internat J Numer Methods Engrg 2007;69(8):1671–716.

[48] Alves de Sousa RJ, Cardoso RP, Fontes Valente RA, Yoon J-W, Grácio JJ, Natal Jorge RM. A new one-point quadrature enhanced assumed strain (EAS) solid-shell element with multiple integration points along thickness: Part I-geometrically linear applications. Internat J Numer Methods Engrg 2005;62(7):952–77.

[49] Alves de Sousa RJ, Cardoso RPR, Fontes Valente RA, Yoon J-W, Grácio JJ, Natal Jorge RM. A new one-point quadrature enhanced assumed strain (EAS) solid-shell element with multiple integration points along thickness—Part II: Nonlinear applications. Internat J Numer Methods Engrg 2006;67(2):160–88.

[50] Chen QQ, Saouab A, Boisse P, Park CH, Bréard J. Woven thermoplastic composite forming simulation with solid-shell element method. Int J Simul Multidiscip Design Optim 2009;3(2):337–41.

[51] Chen Q, Boisse P, Park CH, Saouab A, Bréard J. Intra/inter-ply shear behaviors of continuous fiber reinforced thermoplastic composites in thermoforming processes. Compos Struct 2011;93(7):1692–703.
[52] Xiong H, Guzman Maldonado E, Hamila N, Boisse P. A prismatic solid-shell finite element based on a DKT approach with efficient calculation of through the thickness deformation. Finite Elem Anal Des 2018;151:18–33.
[53] Xiong H, Hamila N, Boisse P. Consolidation modeling during thermoforming of thermoplastic composite prepregs. Mater (Basel, Switzerland) 2019;12(18).
[54] Dia M, Hamila N, Abbas M, Gravouil A. A nine nodes solid-shell finite element with enhanced pinching stress. Comput Mech 2020;65(5):1377–95.
[55] Poppe C, Albrecht F, Krauß C, Kärger L. A 3D modelling approach for fluid progression during process simulation of wet compression moulding – motivation & approach. Procedia Manuf 2020;47:85–92.
[56] Poppe CT, Krauß C, Albrecht F, Kärger L. A 3D process simulation model for wet compression moulding. Compos Part A: Appl Sci Manuf 2021;50(17):106379.
[57] Simon J-W, Stier B, Reese S. A solid-shell finite element for fibre reinforced composites. PAMM 2012;12(1):329–30.
[58] Barfusz O, Smeenk R, Reese S. Solid-shell formulations based on reduced integration - investigations of anisotropic material behaviour at large deformations. PAMM 2018;18(1):201800078.
[59] Schäfer B, Dörr D, Kärger L. Reduced-integrated 8-node hexahedral solid-shell element for the macroscopic forming simulation of continuous fibre-reinforced polymers. Procedia Manuf 2020;47:134–9.
[60] Schäfer B, Dörr D, Kärger L. Potential and challenges of a solid-shell element for the macroscopic forming simulation of engineering textiles. In: ESAFORM 2021. 2021.
[61] Schäfer B, Mitsch J, Kärger L. 3D solid-shell element for macroscopic composite forming simulation enabling thickness prediction. Compos Part A: Appl Sci Manuf 2025;109162.
[62] Mitsch J, Schäfer B, Wank JP, Kärger L. Considering the viscoelastic material behavior in a solid-shell element for thermoforming simulation. In: Material forming: ESAFORM 2024. Materials Research Forum LLC; 2024, p. 457–66.
[63] Mitsch J, Schäfer B, Kärger L. Significance of the material parameters within a three-dimensional solid-shell element for thermoforming simulation. In: Materials research proceedings, vol. 54, Materials Research Forum LLC; 2025, p. 363–72.
[64] Spencer AJM. Continuum theory of the mechanics of fibre-reinforced composites. Vienna: Springer Vienna; 1984.
[65] Spencer A. Theory of fabric-reinforced viscous fluids. Compos Part A: Appl Sci Manuf 2000;31(12):1311–21.
[66] Bertram A. Elasticity and plasticity of large deformations. Cham: Springer International Publishing; 2021.
[67] Belytschko T, Liu WK, Moran B, Elkhodary KI. Nonlinear finite elements for continua and structures. 2. ed., 1. publ. Chichester: Wiley; 2014.
[68] Macosko CW. Rheology: Principles, measurements, and applications. In: Advances in interfacial engineering series, New York NY u.a.: Wiley-VCH; 1994.
[69] Valverde MA, Belnoue JP-H, Kupfer R, Kawashita LF, Gude M, Hallett SR. Compaction behaviour of continuous fibre-reinforced thermoplastic composites under rapid processing conditions. Compos Part A: Appl Sci Manuf 2021;149:106549.
[70] Simo JC, Rifai MS. A class of mixed assumed strain methods and the method of incompatible modes. Internat J Numer Methods Engrg 1990;29(8):1595–638.
[71] Simo JC, Armero F. Geometrically non-linear enhanced strain mixed methods and the method of incompatible modes. Internat J Numer Methods Engrg 1992;33(7):1413–49.
[72] Simo J, Armero F, Taylor R. Improved versions of assumed enhanced strain tri-linear elements for 3D finite deformation problems. Comput Methods Appl Mech Engrg 1993;110:359–86.
[73] Bathe K-J, Dvorkin EN. A formulation of general shell elements-the use of mixed interpolation of tensorial components. Internat J Numer Methods Engrg 1986;22:697–722.
[74] Belytschko T, Leviathan I. Physical stabilization of the 4-node shell element with one point quadrature. Comput Methods Appl Mech Engrg 1994;113(3):321–50.
[75] Betsch P, Stein E. An assumed strain approach avoiding artificial thickness straining for a non-linear 4-node shell element. Commun Numer Methods Eng 1995;11(11):899–909.
[76] Bischoff M, Ramm E. Shear deformable shell elements for large strains and rotations. Internat J Numer Methods Engrg 1997;40(23):4427–49.
[77] Schwarze M, Vladimirov IN, Reese S. On the implementation of the EAS and ANS concept into a reduced integration continuum shell element and applications to sheet forming. Int J Mater Form 2009;2(S1):919–22.
[78] Schäfer BBJ. Macroscopic forming simulation of unidirectional non-crimp fabrics: hyperelastic material modeling and 3D-solid-shell approach (Dissertation), Karlsruher Institut für Technologie (KIT); 2024.
[79] ten Thije RHW, Akkerman R. Solutions to intra-ply shear locking in finite element analyses of fibre reinforced materials. Compos Part A: Appl Sci Manuf 2008;39(7):1167–76.
[80] Hamila N, Boisse P. Locking in simulation of composite reinforcement deformations. Analysis and treatment. Compos Part A: Appl Sci Manuf 2013;53:109–17.
[81] Hamila N, Boisse P. Tension locking in finite-element analyses of textile composite reinforcement deformation. C R Méc 2013;341(6):508–19.
[82] Rohatgi A. WebPlotDigitizer. 2024, [Accessed 17 April 25].
[83] Khan MA, Mabrouki T, Vidal-Sallé E, Boisse P. Numerical and experimental analyses of woven composite reinforcement forming using a hypoelastic behaviour. Application to the double dome benchmark. J Mater Process Technol 2010;210(2):378–88.